

ACOUSTIC POWER TRANSMISSION THROUGH A DUCTED FAN

Ed Envia

Acoustics Branch, NASA Glenn Research Center

edmane.envia-1@nasa.gov

Introduction

For high-speed ducted fans, when the rotor flowfield is shock-free, the main contribution to the inlet radiated acoustic power comes from the portion of the rotor-stator (R/S) interaction acoustic field that is transmitted upstream through the rotor.* Though difficult to verify experimentally using realistic fan hardware, it is generally believed that the fan rotor and the swirling flowfield downstream of it play an important role in determining how much acoustic energy can be transmitted through the rotor into the fan inlet duct. Therefore, for an accurate prediction of the fan inlet noise, the inclusion of the rotor acoustic transmission loss is essential whenever the fan tip relative Mach number is subsonic. Over the years, a number of models have been developed for predicting the acoustic transmission loss through blade rows. These include 2D (or quasi-2D) analytical models as well as 3D high-fidelity computational aeroacoustic (CAA) simulations. The analytic models¹⁻³ tend to be simplistic in their descriptions of the blade row geometry and its flowfield and as such have limited applicability to the real-world fan hardware. The high-fidelity simulations that have been published to date⁴⁻⁶ have not been rigorously applied to realistic rotors and flowfields.[†] The goal of the present study is to use a 3D linearized Euler analysis to carry out a systematic study of acoustic transmission loss through a realistic fan rotor. It is believed that such an analysis captures all the important physical mechanisms of rotor acoustic transmission and yet does not require significant computational resources.

The study described here is focused on the investigation of the blade passing frequency (BPF) tone harmonic transmission loss in a 22-inch model scale fan for which detailed acoustic data have been acquired in a NASA wind tunnel over a wide range of fan tip speeds. The Euler analysis is based on a fairly general three-dimensional linearized inviscid model of the interaction of vortical, acoustic or entropic perturbations with a 3D blade row in axial flow turbomachinery⁷⁻⁹. The mathematical formalism underlying the Euler analysis is expressed as a problem in the frequency domain where the blade row response is computed one BPF harmonic tone at a time. It should be noted that since this analysis models the response of *an individual* blade row to incident perturbations, the fan stage is treated as two separate blade rows. First, the Euler analysis is applied to compute the harmonic acoustic field generated as a result of the impingement of the rotor wakes on the outlet guide vanes (OGV). Then, the model is used again to predict the acoustic transmission (and reflection) of the propagating acoustic field upstream of the OGV as it interacts with the rotor. It should be emphasized that in second application of the analysis, the propagating acoustic field upstream of the OGV is treated as a combination of incident acoustic waves impinging on the rotor

* For supersonic tip relative Mach numbers, the rotor-locked shock system dominates the inlet noise radiation in the form of multiple pure tone (i.e., buzz saw) noise.

† The CAA models described in references 4 and 5 have been used to study acoustic transmission loss for stators, but no similar analyses have been published for rotors. The CAA analysis of rotor acoustic transmission described in reference 6 is carried out in the absence of a mean flow.

from downstream. The difference between the acoustic power levels of given tone upstream of the OGV and upstream of the rotor provide an estimate of the rotor acoustic power transmission loss for that tone. Furthermore, taken together, the resulting analyses predict the tone levels upstream of the fan in the inlet duct and downstream of the OGV in the exhaust duct. These can be compared with the measured inlet and exhaust tone levels to determine the fidelity of this prediction approach.

In the next section a brief description of the benchmark fan stage used in this study and the associated wind tunnel data will be given. This will be followed by a section detailing the prediction strategy used in this study. Next will be a section on the data-theory comparisons and associated discussions. The paper will conclude with a short section on the lessons learned and recommendation for future work.

Benchmark Fan and Experimental Data

The model scale fan stage used in this study is the 22-inch Advanced Ducted Propulsor (ADP), which is a 1990s-vintage design of an ultra-high bypass ratio fan (See Figure 1). The design characteristics of the ADP fan are listed in Table 1. ADP is subsonic at its design tip speed which makes it ideal for the purpose of this study by avoiding the obscuring effects of the buzz saw noise in the inlet. Over the course of three wind tunnel test campaigns since 1996, extensive aerodynamic and acoustic data have been acquired for the ADP fan for a wide range of fan tip speeds all which are considered in this study. These range from 56% to slightly over 108% of the design tip speed (see Table 2). Three additional speeds (6300, 7935 and 9115 RPM) were also added to the cases considered in this study in order to make the increments in the tip speed a bit more uniform. Of course, wind tunnel data for these speeds do not exist. It should be noted that though the ADP fan rig has a simulated (passive) core, the noise associated with fan wakes interacting with the core inlet guide vanes is a minor component of the ADP sound field and is ignored here.

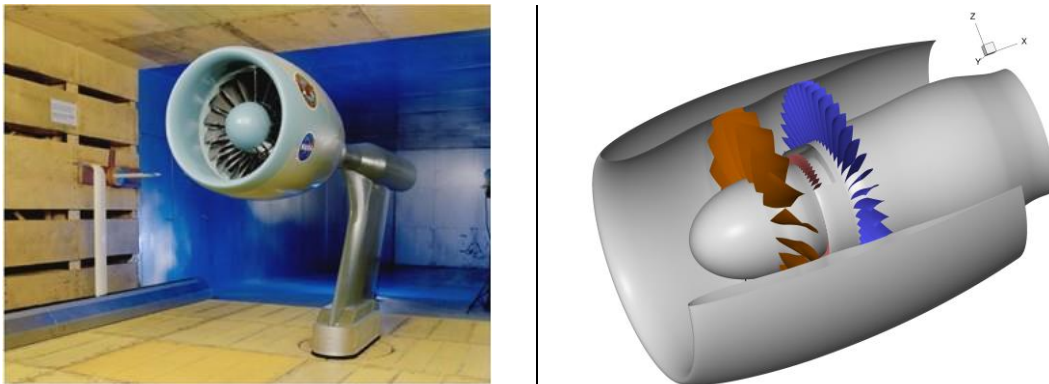


Figure 1. The 22-inch model scale ADP fan shown installed in the test section of the NASA 9' x 15' Low-Speed Acoustic Wind Tunnel shown (left) and its cutaway (right) shown on the right. The ADP fan has 18 fan blades, 45 bypass outlet guide vanes and 63 core inlet guide vanes.

Table 1: The ADP stage fan design parameters.

Parameter	ADP Fan
Rotor Diameter, in. (m)	22 (0.56)
Corrected Tip Speed, ft/s (m/s)	840 (256)
Stage Pressure Ratio	1.29
Rotor Hub-to-Tip Radius Ratio	0.43
Bypass Ratio	13.3
Mass Flow, lbm/s (kg/s)	85.7 (38.9)
Rotor Blade Count	18
Bypass Outlet Guide Vane Count	45
Core Inlet Guide Vane Count	63

Table 2: The fan speeds considered in this study.

Condition	Corrected RPM	% Design Speed
—	4950	56.6
Approach	5425	62.0
—	5900	67.4
—	6300	72.0
—	6700	76.6
—	7030	80.0
Cutback	7525	86.0
—	7935	90.1
—	8345	95.4
Sideline	8750	100.0
—	9115	104.2
—	9480	108.3

The aerodynamic and acoustic data for the ADP fan were acquired in the NASA 9-ft by 15-ft Low-Speed Acoustic Wind Tunnel which is a continuous-flow, anechoic tunnel capable of simulating flight speeds of up to Mach 0.23. The test section is acoustically treated and is anechoic down to 250 Hz⁷, a limit which is well below all of the tone frequencies considered in this study. All fan acoustic data used in this study were acquired at the tunnel Mach number of 0.1. The test layout is depicted in Figure 2, which shows the plan view of the wind tunnel with the fan stage installed. The acoustic data were acquired using a ¼-inch (0.64-cm) traversing microphone that moves on a sideline track that is parallel to, and displaced horizontally 89.3 inches (2.27 m) from, the vertical symmetry plane of the fan. The traversing microphone is located at the same height from the tunnel floor as the fan rotational axis. Acoustic pressure data were acquired at 48 positions (i.e., sideline angles) along the traverse track at approximately 2.5° intervals. The sideline (i.e., polar) angle θ is defined such that upstream infinity is at 0°. The range of sideline angles subtended by the track is from 27° to 135°. To extend the aft angular coverage three fixed microphones were also used as shown in Figure 2. These microphones provide additional polar angle measurements at 140°, 150°, and 160°.

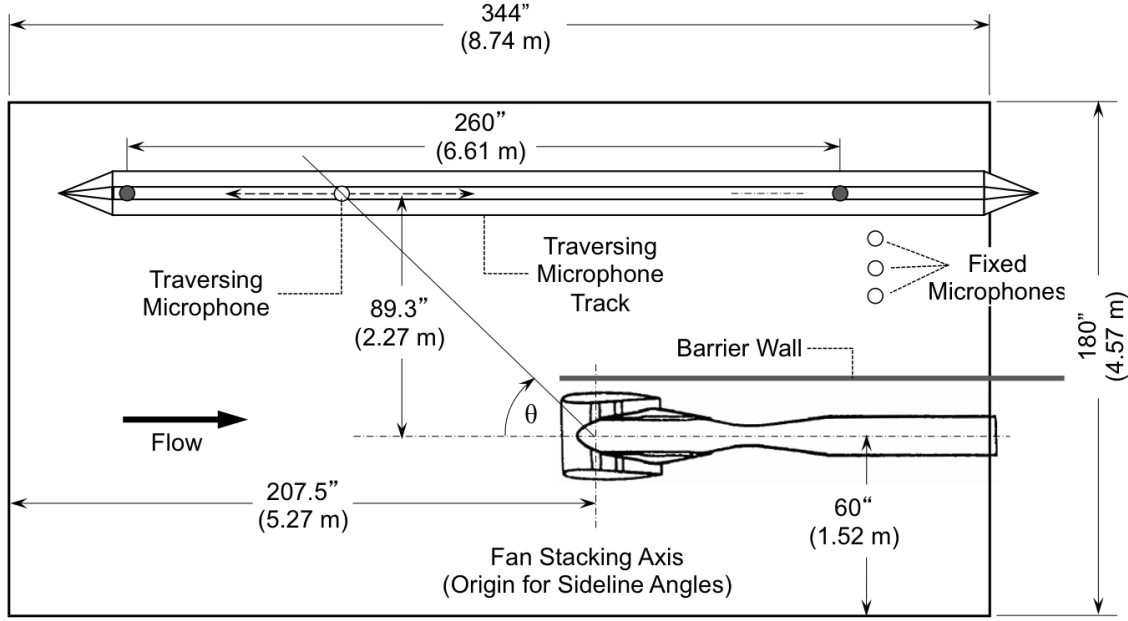


Figure 2. Plan view of the 9' × 15' wind tunnel test section showing the model fan, traversing microphone, and fixed microphones. Dimensions are in inches (meters).

The acoustic data were acquired both with, and without, a barrier wall in order to isolate inlet- and exhaust-radiated noise contributions. The barrier wall extends vertically from the floor to the ceiling of the tunnel. As indicated in Figure 2, when the barrier wall is in place, the aft microphone locations are shielded from the fan exhaust noise and only inlet-radiated noise is measured. Without the wall, the microphones measure contributions from both the inlet and exhaust. The difference between the two provides a good estimate of the exhaust-radiated noise.

The microphone data were made “loss-less” by correcting for the effects of humidity (i.e., atmospheric absorption of acoustic signals). The lossless r.m.s. microphone data were converted to sound pressure level (SPL) using the standard reference pressure of 2×10^{-5} Pa. Sideline SPL were projected onto a sphere and integrated over the polar angle range[‡] to calculate the radiated acoustic power level (PWL) using the standard reference power level of 10^{-12} Watts. The acoustic power calculations for the inlet were carried out on a sphere centered on the point at the intersection of the fan highlight plane and the fan rotational axis. The range of polar angle integration is from 0° to 90°. Similarly, for the exhaust power level calculations, the SPLs were projected on a sphere centered on the point at the intersection of the fan nozzle plane and the fan rotational axis and integrated over the polar angle range 90° to 180°.

ADP, like all modern fan stages, has a cut-off fan outlet guide vane (OGV) design, which implies that the BPF tone is nominally cut-off and the principal propagating tone is 2BPF. This tone is the focus of this study. The Tyler-Sofrin rule⁸ for the 2BPF tone, given by the expression $m = 2B - kV$ (where B is the blade count, V the vane count, and k an arbitrary integer), determines the circumferential mode content of this tone. In theory, only $k = 1$ (i.e., $m = -9$) corresponds to a circumferential mode with propagating radial mode content both in the inlet and exhaust. This is

[‡] It is assumed that the acoustic field is azimuthally symmetric.

borne out by the measured circumferential modal content for ADP obtained using the rotating rake measurement system⁹ which shows that the $m = -9$ is the dominant circumferential mode at 2BPF in terms of both SPL and PWL. It should be noted here that due to imperfection in the manufacture and installation (i.e., blade stagger) of the rotor blades and stator vanes, the sound field at 2BPF also contains a number of extraneous circumferential orders distributed on either side of the $m = -9$. These modes contain some modest power levels and thus ‘contaminate’ the measured sideline data to some extent. It is difficult to isolate their effects and, as such, some baseline discrepancy is inevitable between the measured and the theoretically predicted 2BPF tone levels since the theory assumes that the blades and vanes in each blade row are perfectly identical in geometry and installation.

Acoustic Prediction Methodology

As was discussed before, the aeroacoustic prediction methodology used in this study is based on a linearized Euler analysis of a 3D blade response to incident vortical, acoustic or entropic perturbations. The theoretical model is embodied in a NASA code called LINFLUX¹⁰⁻¹², which requires a three-dimensional steady, nonlinear, inviscid base flow for the target blade row. Detailed description of the mathematical underpinning of the LINFLUX code can be found in references 10 through 12, but in the interest of completeness an outline of the underlying mathematical formulation is given below. Much of the material is taken directly from the reference 9.

The nonlinear equations governing the unsteady flow through a blade row rotating with the angular velocity Ω [§], written in the integral form in the frame reference fixed to the blade row can be written in the compact form

$$\frac{d}{dt} \int_{\mathcal{V}} \tilde{\mathbf{U}} d\mathcal{V} + \int_{\mathcal{A}} \left[\tilde{\mathbf{F}}_{x_j} - \tilde{\mathbf{U}} \dot{\mathcal{R}}_{x_j} \right] n_{x_j} d\mathcal{A} = \int_{\mathcal{V}} \tilde{\mathbf{S}} d\mathcal{V}, \quad (1)$$

where the symbol \sim indicates a time-dependent quantity, $\mathcal{V}(t)$ denotes an arbitrarily moving control volume bounded by the control surface $\mathcal{A}(\mathbf{x}, t)$, and $\mathbf{n} = (n_{x_1}, n_{x_2}, n_{x_3})$ is the unit vector normal to the surface \mathcal{A} and pointing outward from volume \mathcal{V} . The vector $\mathcal{R}(\bar{\mathbf{x}}, t) = (\mathcal{R}_{x_1}, \mathcal{R}_{x_2}, \mathcal{R}_{x_3})$ denotes the displacement of a fluid particle (in the blade row frame of reference) from its mean position $\bar{\mathbf{x}}$ with $\mathbf{x} = \bar{\mathbf{x}} + \mathcal{R}(\bar{\mathbf{x}}, t)$ denoting its instantaneous position. Therefore, $\dot{\mathcal{R}}(\bar{\mathbf{x}}, t)$ indicates the rate of change of the displacement with time (that is, its velocity).

The vector quantities $\tilde{\mathbf{U}}$, $\tilde{\mathbf{F}}_{x_j}$ and $\tilde{\mathbf{S}}$ denote, respectively, the state, flux and source vectors with the source term accounting for the rotation of the frame of reference. These terms are given by

[§] For a stator $\Omega \equiv 0$.

$$\tilde{\mathbf{U}} = \begin{bmatrix} \tilde{\rho} \\ \tilde{\rho}\tilde{V}_{x_1} \\ \tilde{\rho}\tilde{V}_{x_2} \\ \tilde{\rho}\tilde{V}_{x_3} \\ \tilde{\rho}\tilde{E}_T \end{bmatrix}, \quad \tilde{\mathbf{F}}_{x_j}(\tilde{\mathbf{U}}) = \begin{bmatrix} \tilde{U}_{j+1} \\ \tilde{U}_{j+1}\tilde{U}_2/\tilde{U}_1 + \tilde{P}\delta_{1j} \\ \tilde{U}_{j+1}\tilde{U}_3/\tilde{U}_1 + \tilde{P}\delta_{2j} \\ \tilde{U}_{j+1}\tilde{U}_4/\tilde{U}_1 + \tilde{P}\delta_{3j} \\ \tilde{U}_{j+1}(\tilde{U}_5 + \tilde{P})/\tilde{U}_1 \end{bmatrix}, \quad \tilde{\mathbf{S}}(\tilde{\mathbf{U}}, \mathbf{x}) = \begin{bmatrix} 0 \\ 0 \\ \Omega^2\tilde{U}_1x_2 + 2\Omega\tilde{U}_4 \\ \Omega^2\tilde{U}_1x_3 - 2\Omega\tilde{U}_3 \\ \Omega^2(\tilde{U}_3x_2 + \tilde{U}_4x_3) \end{bmatrix}, \quad (2)$$

where $\tilde{\rho}$, $\tilde{\mathbf{V}}$, $\tilde{E}_T = \tilde{E} + \tilde{V}^2/2$ and $\tilde{P} = (\gamma - 1)\tilde{\rho}\tilde{E} = (\gamma - 1)[\tilde{U}_5 - \tilde{U}_1^{-1}(\tilde{U}_2^2 + \tilde{U}_3^2 + \tilde{U}_4^2)/2]$ are the density, velocity, specific internal energy, and pressure. Naturally, the velocity and internal energy are measured relative to the blade row frame of reference.

The differential form of Eq. (1), which applies at fixed locations ($\mathcal{R} \equiv 0$), is needed to describe the unsteady flow at the inflow and outflow boundaries. Expressed in cylindrical coordinates, i.e., $\xi = x_1$, $r = (x_2^2 + x_3^2)^{1/2}$, $\theta = -\tan^{-1} x_2/x_3$, this equation has the form

$$\frac{\partial \bar{\mathbf{U}}^{\text{cyl}}}{\partial t} + \frac{1}{r} \frac{\partial(r\tilde{\mathbf{F}}_r)}{\partial r} + \frac{1}{r} \frac{\partial \tilde{\mathbf{F}}_\theta}{\partial \theta} + \frac{\partial \tilde{\mathbf{F}}_\xi}{\partial \xi} = \tilde{\mathbf{S}}, \quad (3)$$

$$\tilde{\mathbf{U}}^{\text{cyl}} = \begin{bmatrix} \tilde{\rho} \\ \tilde{\rho}\tilde{V}_r \\ \tilde{\rho}\tilde{V}_\theta \\ \tilde{\rho}\tilde{V}_\xi \\ \tilde{\rho}\tilde{E}_T \end{bmatrix}, \quad \tilde{\mathbf{S}}(\tilde{\mathbf{U}}, \mathbf{x}) = \begin{bmatrix} 0 \\ (\tilde{U}_3^{\text{cyl}})^2/\tilde{U}_1^{\text{cyl}} + \tilde{P} \\ -\tilde{U}_2^{\text{cyl}}\tilde{U}_3^{\text{cyl}}/\tilde{U}_1^{\text{cyl}} \\ 0 \\ 0 \end{bmatrix} + \Omega \begin{bmatrix} 0 \\ 2\tilde{U}_3^{\text{cyl}} + \tilde{U}_1^{\text{cyl}}\Omega r \\ -2\tilde{U}_2^{\text{cyl}} \\ 0 \\ \tilde{U}_2^{\text{cyl}}\Omega r \end{bmatrix}. \quad (4)$$

The flux vectors $\tilde{\mathbf{F}}_r(\tilde{\mathbf{U}}^{\text{cyl}})$, $\tilde{\mathbf{F}}_\theta(\tilde{\mathbf{U}}^{\text{cyl}})$, $\tilde{\mathbf{F}}_\xi(\tilde{\mathbf{U}}^{\text{cyl}})$, and pressure $\tilde{P}(\tilde{\mathbf{U}}^{\text{cyl}})$ have functional forms similar to those indicated for $\tilde{\mathbf{F}}_{x_j}(\tilde{\mathbf{U}})$ in Eq. (2) and $\tilde{P}(\tilde{\mathbf{U}})$ given above.

These field equations must be supplemented by boundary conditions on the blade surfaces, the duct walls and the inflow ($\xi = \xi_-$) and outflow ($\xi = \xi_+$) planes. Flow tangency conditions,

$$(\tilde{\mathbf{V}} - \dot{\mathcal{R}}) \cdot \mathbf{n} = 0 \quad \text{for } \mathbf{x} \in \mathcal{B}_n, \quad r = r_H, \quad r = r_D, \quad (5)$$

apply at the blade surfaces \mathcal{B}_n and stationary duct walls $r = r_H$, $r = r_D$. In addition, time-averaged and circumferentially-averaged values of total pressure, total temperature and inlet flow angle are specified as a function of radius at the domain's inflow and outflow boundaries, and the time-averaged and circumferentially-averaged static pressure is specified at the outflow boundary consistent with the radial equilibrium. Unsteady departures from these average values at the inlet

and/or exit planes are additional information that must be supplied in order to solve the governing equations for the unsteady field in the domain. For the R/S interaction problem, these are the harmonic wake perturbations specified at the inflow plane for the OGV domain. For the acoustic transmission problem, these are the upstream propagating acoustic waves specified at the outflow plane of the rotor domain.

The relevant domains for the ADP fan are shown in Figure 3 below. The domains extend roughly one airfoil axial chord upstream and downstream of the target blade row. As can be seen in the figure, due to the presence of the flowpath splitter for ADP there is an area change between the inflow plane of the OGV domain and outflow plane of the rotor domain. The area change is less than 1.3% and is ignored here. In fact, the presence of the splitter in the rotor domain is also ignored as is the presence of the core IGV.

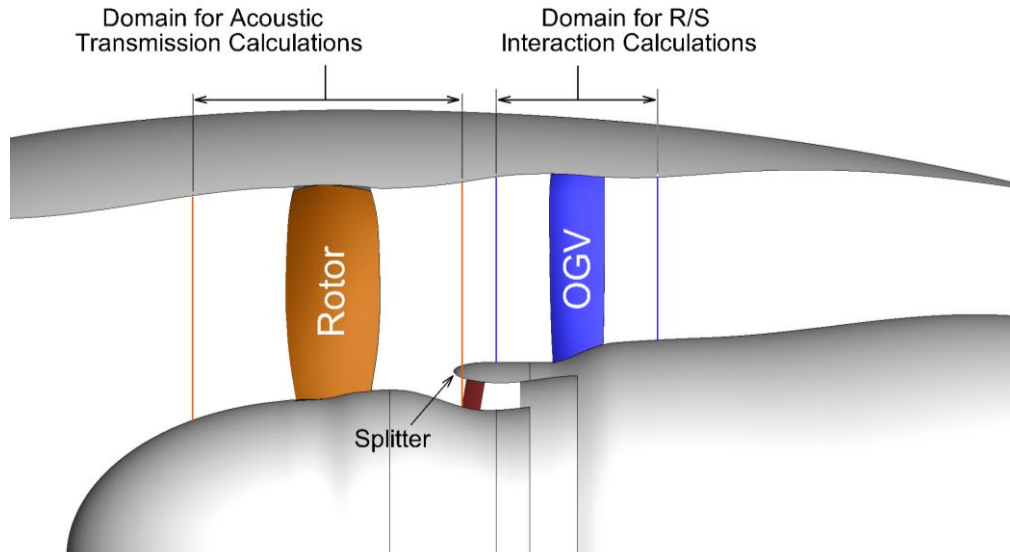


Figure 3. Domains of interest for the aeroacoustic analyses. The *OGV* domain is used for computing tone noise generated by the R/S interaction. The *Rotor* domain is used for acoustic transmission calculations.

Assuming that unsteady rotor wake perturbations are small harmonic fluctuations compared with the time-averaged flow, one can expand the unsteady state vector in the asymptotic series

$$\tilde{\mathbf{U}}(\mathbf{x}, t) = \mathbf{U}(\bar{\mathbf{x}}) + \tilde{\mathbf{u}}(\mathbf{x}, t) + \dots \approx \mathbf{U}(\bar{\mathbf{x}}) + \text{Re}\left\{ \mathbf{u}(\mathbf{x}) e^{i\omega t} \right\}, \quad (6)$$

where the state vectors $\mathbf{U}(\bar{\mathbf{x}})$ and $\tilde{\mathbf{u}}(\mathbf{x}, t)$ denote the conservation variables for the steady background flow and the first-order (i.e., linear) unsteady perturbations. The vector $\mathbf{u}(\mathbf{x})$ in the last term on the right hand side of Eq. (6) contains the complex amplitudes of the conservation variables $(\rho, \bar{\rho}v_{x_1} + \rho V_{x_1}, \bar{\rho}v_{x_2} + \rho V_{x_2}, \bar{\rho}v_{x_3} + \rho V_{x_3}, \bar{\rho}e_T + \rho E_T)$ where $(\bar{\rho}, \mathbf{V}, E_T)$ denote the steady primitive flow variables and $(\rho, \mathbf{v}, \mathbf{e}_T)$ denote the unsteady complex amplitudes of the first order primitive variables. The unsteady flux and source vectors in Eq. (1) can similarly be expanded as follows

$$\tilde{\mathbf{F}}_{x_j}(\tilde{\mathbf{U}}) = \mathbf{F}_{x_j}(\mathbf{U}) + \frac{\partial \mathbf{F}_{x_j}}{\partial \mathbf{U}} \tilde{\mathbf{u}} + \dots, \quad \tilde{\mathbf{S}}(\tilde{\mathbf{U}}, \mathbf{x}) = \mathbf{S}(\mathbf{U}, \bar{\mathbf{x}}) + \frac{\partial \mathbf{S}}{\partial \mathbf{U}} \tilde{\mathbf{u}} + (\mathcal{R} \cdot \nabla_{\bar{\mathbf{x}}}) \mathbf{S} + \dots \quad (7)$$

It is most convenient to express the governing equations for the steady and unsteady flows in terms of the mean or steady state quantities $\bar{\mathcal{V}}$, $\bar{\mathcal{A}}$ and $\bar{\mathbf{x}}$. This would necessitate spatial transformations of the various operators in the governing equations. These linearized versions of these transformation are as follows

$$\frac{d}{dt} \int_{\mathcal{V}} (\) d\mathcal{V} = \int_{\bar{\mathcal{V}}} \left[\frac{\partial (\)}{\partial t} \Big|_{\bar{\mathbf{x}}} + (\) \nabla_{\bar{\mathbf{x}}} \cdot \dot{\mathcal{R}} d\bar{\mathcal{V}} \right] d\bar{\mathcal{V}} + \dots, \quad \frac{\partial}{\partial t} \Big|_{\mathbf{x}} = \frac{\partial}{\partial t} \Big|_{\bar{\mathbf{x}}} + \dot{\mathcal{R}}_{\bar{x}_k} \frac{\partial}{\partial \bar{x}_k} + \dots \quad (8)$$

Substituting the linearized versions of the operators from Eq. (8) in Eq. (1) and equating terms of like power in the perturbations lead to a set of nonlinear steady state equations for the mean flow and a set of linear, variable-coefficient equations for the perturbations. The mean flow equations reduce to

$$\int_{\bar{\mathcal{A}}} \mathbf{F}_{\bar{x}_j} n_{x_j} d\bar{\mathcal{A}} = \int_{\bar{\mathcal{V}}} \mathbf{S} d\bar{\mathcal{V}}, \quad (9)$$

subject to the flow tangency conditions

$$\mathbf{V} \cdot \mathbf{n} = 0 \quad \text{for } \bar{\mathbf{x}} \in \mathcal{B}_n, \quad r = r_H, \quad r = r_D, \quad (10)$$

and the circumferential periodicity conditions

$$\bar{\rho}(\bar{r}, \bar{\theta} + 2\pi n / N, \bar{\xi}) = \bar{\rho}(\bar{r}, \bar{\theta}, \bar{\xi}), \quad \mathbf{V}(\bar{r}, \bar{\theta} + 2\pi n / N, \bar{\xi}) = \mathbf{T}_n \mathbf{V}(\bar{r}, \bar{\theta}, \bar{\xi}), \quad (11)$$

which apply outside of the blade passage on the circumferential boundaries of the computational domain. In these equations N is the number of blade or vane passages and \mathbf{T}_n is the rotation matrix which relates a vector in the reference passage (say, $n = 0$) to its counterpart in the n^{th} passage with $n = 0, 1, 2, \dots, N-1$.

These conditions are supplemented by the circumferentially averaged steady state total pressure, temperature and flow angle at the inflow plane and the circumferentially averaged static pressure at the outflow boundary.

The corresponding set of linear equations governing the evolution of the harmonic perturbations are given by

$$\begin{aligned}
& i\omega \int_{\bar{\mathcal{V}}} \mathbf{u} d\bar{\mathcal{V}} + \int_{\bar{\mathcal{A}}} \left(\frac{\partial \mathbf{F}_{x_j}}{\partial \mathbf{U}} \mathbf{u} \right) \bar{n}_{x_j} d\bar{\mathcal{A}} - \int_{\bar{\mathcal{V}}} \frac{\partial \mathbf{S}}{\partial \mathbf{U}} \mathbf{u} d\bar{\mathcal{V}} = \\
& -i\omega \int_{\bar{\mathcal{V}}} \left(\frac{\partial \mathcal{R}_{\bar{x}_k}}{\partial \bar{x}_k} \right) \mathbf{U} d\bar{\mathcal{V}} + \int_{\bar{\mathcal{A}}} \left[i\omega \mathcal{R}_{\bar{x}_j} \bar{n}_{x_j} \mathbf{U} d\bar{\mathcal{A}} - \mathbf{F}_{x_j} \Delta (\bar{n}_{x_j} d\bar{\mathcal{A}}) \right] + \int_{\bar{\mathcal{V}}} \frac{\partial}{\partial \bar{x}_j} (\mathcal{R}_{\bar{x}_j} \mathbf{S}) d\bar{\mathcal{V}},
\end{aligned} \tag{12}$$

supplemented by the linearized tangency conditions,

$$\mathbf{v} \cdot \mathbf{n} = i\omega \mathcal{R} \cdot \mathbf{n} + \mathbf{V} \cdot \nabla(\mathcal{R} \cdot \mathbf{n}) \quad \text{for } \bar{\mathbf{x}} \in \mathcal{B}_n, \quad r = r_H, \quad r = r_D. \tag{13}$$

The circumferential periodicity conditions are given by

$$\rho(\bar{r}, \bar{\theta} + 2\pi n / N, \bar{\xi}) = \rho(\bar{r}, \bar{\theta}, \bar{\xi}), \quad \mathbf{v}(\bar{r}, \bar{\theta} + 2\pi n / N, \bar{\xi}) = \mathbf{T}_n \mathbf{v}(\bar{r}, \bar{\theta}, \bar{\xi}) e^{in\sigma}, \tag{14}$$

where $\sigma = 2\pi N_D / N$ is the inter-blade phase angle and N_D denotes the circumferential periodicity of the incident disturbance. The sign of N_D depends on the direction in which the disturbance rotates circumferentially with respect to the direction of θ coordinate. Eqs. (9) and (12) must be solved numerically in order to compute the steady and unsteady field solutions**.

Finally, the differential equations that describe the steady and linearized unsteady flows at the inflow and outflow boundaries have the form

$$\frac{1}{r} \frac{\partial(r\mathbf{F}_r)}{\partial r} + \frac{1}{r} \frac{\partial \mathbf{F}_\theta}{\partial \theta} + \frac{\partial \mathbf{F}_\xi}{\partial \xi} = \mathbf{S}, \tag{15}$$

$$i\omega \mathbf{u} + \frac{1}{r} \frac{\partial(r\mathbf{A}\mathbf{u})}{\partial r} + \frac{1}{r} \frac{\partial(\mathbf{B}\mathbf{u})}{\partial \theta} + \frac{\partial(\mathbf{C}\mathbf{u})}{\partial \xi} - \mathbf{D}\mathbf{u} = 0, \tag{16}$$

where $\mathbf{A} = \partial \mathbf{F}_r / \partial \mathbf{U}^{\text{cyl}}$, $\mathbf{B} = \partial \mathbf{F}_\theta / \partial \mathbf{U}^{\text{cyl}}$ and $\mathbf{C} = \partial \mathbf{F}_\xi / \partial \mathbf{U}^{\text{cyl}}$ are the flux Jacobian matrices and $\mathbf{D} = \partial \mathbf{S} / \partial \mathbf{U}^{\text{cyl}}$ is the source term Jacobian.

To determine the outgoing perturbations at the inflow and outflow boundaries of the computational domain, it is necessary to match the three-dimensional field solutions to Eq. (12) to the solutions given by Eq. (15). This is done in an approximate manner as follows. We assume that, far from the blade row, the duct radii r_H and r_D are constant, and, that the circumferentially averaged steady flow depends only on the radius. As a result of these assumptions, it follows that the steady flow has only axial and tangential velocity components, but no radial velocity

** In the interest of brevity, the details of the numerical procedure will not be discussed here. The reader is referred to references 13 through 15 for an in-depth description of the numerical algorithms.

component. Furthermore, it can be shown that $dP/dr = \bar{\rho}(\bar{V}_\theta^{\text{abs}})^2/r$. Consequently, Eq. (16) simplifies to

$$i\omega\mathbf{u} + \frac{1}{r} \frac{\partial(r\mathbf{A}_2\mathbf{u})}{\partial r} + \frac{1}{r} \mathbf{B}_2 \frac{\partial\mathbf{u}}{\partial\theta} + \mathbf{C}_3 \frac{\partial\mathbf{u}}{\partial\xi} - \mathbf{D}_2\mathbf{u} = 0, \quad (17)$$

This equation describes the approximate first-order perturbations far from the blade row. The subscript 2 on the Jacobin matrices indicates that they are evaluated under the condition of zero steady radial velocity, i.e., $U_2^{\text{cyl}} = \bar{\rho}\bar{V}_r$ (e.g., $\mathbf{A}_2 \equiv \partial\mathbf{F}_r / \partial\mathbf{U}^{\text{cyl}}|_{U_2^{\text{cyl}}=0}$).

Since the steady axial and tangential velocity components in Eq. (17) are functions of radius only, it transpires that the solution to Eq. (17) can be described in terms of an independent family of entropic disturbances and weakly coupled families of nearly acoustic and nearly vortical disturbance^{††}. Since from a numerical point of view it is quite challenging to represent an arbitrary unsteady field in terms of coupled families of nearly acoustic and nearly vortical disturbances, further approximations are necessary if progress is to be made. In the LINFLUX code, the weak coupling is ignored and the disturbances are modeled as a family of acoustically dominated modal disturbances and a “convected” disturbance field that represents vortical and/or entropic disturbances. In other words, it is assumed that $\mathbf{u} = \mathbf{u}_A + \mathbf{u}_C$ where \mathbf{u}_A represents the modal acoustic perturbations and \mathbf{u}_C the convected and/or entropic perturbations. The state vector \mathbf{u}_C is prescribed at the inflow boundary^{‡‡} as an approximate solution of the Eq. (17), and is convected through the domain according to $\bar{D}\mathbf{u}_C / Dt = 0$. The individual members of the family of acoustic disturbances \mathbf{u}_A are assumed to have the modal form $\mathbf{u} = \mathbf{u}_{mn}^R(r)\exp(\chi_{mn}\xi + im\theta)$, where χ_{mn} and m are the axial and circumferential wavenumbers of the disturbance and the superscript R denotes the right eigenvectors. Substituting this in Eq. (17) yields a system of homogeneous ordinary differential equations of the form

$$i\omega\mathbf{I}\mathbf{u}_{mn}^R + \frac{1}{r} \frac{d}{dr}(r\mathbf{A}_2\mathbf{u}_{mn}^R) + \frac{im}{r} \mathbf{B}_2\mathbf{u}_{mn}^R + \chi_{mn} \mathbf{C}_2\mathbf{u}_{mn}^R - \mathbf{D}_2\mathbf{u}_{mn}^R = 0. \quad (18)$$

where \mathbf{I} is the identity matrix. This system of equations can be discretized using the standard finite difference methods and solved using the usual methods. Applying the impermeable duct wall boundary condition $v_r = 0$ (for hard wall ducts) we arrive at the discretized matrix equation

$$(\mathbf{P} - \chi_{mn} \mathbf{C}_2)\mathbf{u}_{mn}^R = 0, \quad (19)$$

where $\mathbf{P} = i\omega\mathbf{I} - \mathbf{L}(r, \mathbf{A}_2) - im\mathbf{B}_2/r + \mathbf{D}_2$ and $\mathbf{L}(r, \mathbf{A}_2)$ is a finite difference approximation to $r^{-1}d(r\mathbf{A}_2\mathbf{u}_{mn}^R)/dr$. Eq. 19 is solved using a standard linear algebra routine to determine the axial

^{††} This is true only if the steady flow was further assumed to be isentropic.

^{‡‡} For example, as the harmonic components of the rotor wake for R/S interaction at the inflow plane of the OGV domain.

eigenvalues χ_{mn} and the associated right eigenvectors \mathbf{u}_{mn}^R representing the acoustic modal disturbances at the domain boundaries. The left eigenvectors \mathbf{u}_{mn}^L are determined by solving the equations $(\mathbf{P} - \chi_{mn} \mathbf{C}_2)^H \mathbf{u}_{mn}^L = 0$, where the superscript H denotes the conjugate transpose. An orthonormal set of left eigenvectors can be formed by setting $(\mathbf{v}_{mn}^L)^H = (\mathbf{u}_{mn}^L)^H \mathbf{C}_2 / [(\mathbf{u}_{mn}^L)^H \mathbf{C}_2 \mathbf{u}_{mn}^R]$. A more detailed description of the solution procedure for equation 19 can be found in reference 9.

The numerical solution to Eq. (19) may contain spurious modes, which must be eliminated in order to arrive at a valid solution. In addition, both acoustic and convected disturbances can emerge as solutions to Eq. (19). The group velocity

$$V_{g,mn} = \frac{\partial \omega}{\partial \chi_{mn}} = \frac{\langle \mathbf{v}_{mn}^L, \mathbf{C}_2 \mathbf{u}_{mn}^R \rangle}{\langle \mathbf{v}_{mn}^L, (\partial \mathbf{P} / \partial \omega) \mathbf{u}_{mn}^R \rangle}, \quad (20)$$

i.e., the velocity at which a propagating modal disturbance carries energy, can be used to distinguish between such solutions. Nearly-convected disturbances travel downstream at axial speeds slightly less than or slightly more than the mean flow speed. On the other hand, the acoustic disturbances travel both upstream and downstream at the speed of sound relative to the flow. Therefore, if the solution of Eq. (18) yields any mode(s) not travelling at the speed of sound, they should be eliminated since the state vector \mathbf{u}_c is supposed to contain all convected nearly-disturbances.

After the spurious and nearly convected modes have been eliminated, the remaining eigenvectors can be combined to construct the outgoing acoustic state vector \mathbf{u}_A in terms of a finite double sum,

$$\mathbf{u}_A(r, \theta, \xi) = \sum_m e^{im\theta} \sum_n \left[a_{mn}^- \mathbf{u}_{mn}^{R,-}(r) e^{\chi_{mn}^- \xi} + a_{mn}^+ \mathbf{u}_{mn}^{R,+}(r) e^{\chi_{mn}^+ \xi} \right], \quad \chi_{mn}^\mp = \beta_{mn}^\mp + i\kappa_{mn}^\mp, \quad (21)$$

where the upstream and downstream propagating modes are distinguished by the superscripts $-$ and $+$, respectively. a_{mn}^\mp denote the complex modal amplitude associated with each eigenvector. A mode for which β_{mn}^\mp is zero is propagating; otherwise the mode is evanescent and decays exponentially with distance. The index n ($= 0, 1, 2, \dots$) enumerates the radial modes in each circumferential mode order.

The modal amplitudes a_{mn}^\mp are determined by taking inner products involving the left eigenvectors \mathbf{v}_{mn}^L and the state vector \mathbf{u} , i.e.,

$$a_{mn}^\mp = \langle \mathbf{v}_{mn}^{L,\mp}, \frac{N}{2\pi} \int_\theta^{\theta+2\pi} \mathbf{u} e^{-im\theta} d\theta \rangle = \frac{1}{r_D - r_H} \int_{r_H}^{r_D} (\mathbf{v}_{mn}^{L,\mp})^H \left[\frac{N}{2\pi} \int_\theta^{\theta+2\pi} \mathbf{u} e^{-im\theta} d\theta \right] dr. \quad (22)$$

The implied assumption here is that the inner products $\langle \mathbf{v}_{mn}^{L,\mp}, \mathbf{u}_c \rangle$ are negligible; that is to say the left eigenvectors of the acoustic disturbances are nearly orthogonal to the convected disturbances. This concludes the description of the theoretical underpinnings of the LINFLUX code.

To summarize, the solution procedure is as follows. First the nonlinear steady mean flow equations for density, momenta and total energy, i.e., Eq. (9), must be solved. This is most conveniently done by using a code called TURBO¹³, which, like LINFLUX, is a finite-volume code and uses the same grid topology and, in fact, the same computational domain and grid as LINFLUX. With the mean flow computed, the linearized perturbation equations, i.e., Eq. (12), are solved for the field solution of the first order density, momenta and total energy perturbations. The perturbation solution is then inserted in Eq. (22) to compute the complex amplitudes of the outgoing acoustic modes, a_{mn}^{\mp} . Naturally, the inner product denoted by Eq. (22) can be calculated only after the eigenvalue problem described by Eq. (18) is solved. The end results of this chain of computations are the outgoing acoustic modes at the inflow and outflow boundaries of the computational domain. These acoustic modes include a set of propagating modes as well as a small set of the least damped evanescent modes. As a standard output, LINFLUX computes modal SPL and PWL for the propagating acoustic modes and these are the quantities that can be compared with the experimental data.

To compute SPL and PWL it is necessary to calculate both the time-average and area-average of the acoustic pressure at the inflow and outflow planes. The time-averaging is straightforward and is given by

$$\langle\tilde{a}\tilde{b}\rangle = \frac{2}{2\pi} \int_0^{2\pi} \tilde{a}\tilde{b}d(\omega t) = \frac{1}{4}(ab^* + \tilde{a}^*\tilde{b}) = \frac{1}{2}\text{Re}\{ab^*\}, \quad (23)$$

where \tilde{a} and \tilde{b} denote two first-order unsteady flow variables. The area-average is then given by

$$\langle\langle\tilde{a}\tilde{b}\rangle\rangle = A_D^{-1} \int_{A_D} \langle ab^* \rangle dA_D = \frac{1}{2} A_D^{-1} \text{Re} \left\{ \int_{r_H}^{r_D} \int_0^{2\pi} ab^* r dr d\theta \right\}, \quad (24)$$

where $A_D = \pi(r_D^2 - r_H^2)$ is the duct cross-sectional area. Since the description of the acoustic field is given in terms of modes (see Eq. 21), the product ab^* for pressure has the form

$$ab^* = \sum_m \sum_n \sum_{m'} \sum_{n'} a_{mn} (a_{m'n'})^* \Phi_{mn}^a (\Phi_{m'n'}^b)^* e^{i(m-m')\theta + (\chi_{mn} + \chi_{m'n'}^*)\xi}, \quad (25)$$

where a_{mn} & $a_{m'n'}$ denote the complex-valued mode amplitudes, and Φ_{mn}^a & $\Phi_{m'n'}^b$ denote the radial shapes of modes (recall that these are known only numerically^{§§}). Substituting Eq. (25) in Eq. (24) and integrating with respect to θ , we arrive at

$$\langle\langle\tilde{a}\tilde{b}\rangle\rangle = \pi A_D^{-1} \operatorname{Re} \left\{ \sum_{\text{Prop.: } m,n,n'} a_{mn} (a_{mn'})^* e^{i(\kappa_{mn} - \kappa_{mn'})\xi} \int_{r_H}^{r_D} \Phi_{mn}^a (\Phi_{m'n'}^b)^* r dr \right\}. \quad (26)$$

where the summation is over only the propagating modes. Unlike the uniform flow duct modes, the integrals in Eq. (26) do not, in general, vanish when $n = n'$. Instead, $\langle\langle\tilde{a}\tilde{b}\rangle\rangle$ will vary harmonically with ξ . For a definitive result, we compute the axial mean value of $\langle\langle\tilde{a}\tilde{b}\rangle\rangle$, which is given by

$$\langle\langle\langle\tilde{a}\tilde{b}\rangle\rangle\rangle = \pi A_D^{-1} \operatorname{Re} \left\{ \sum_{\text{Prop.: } m,n,n'} |a_{mn}|^2 \int_{r_H}^{r_D} \Phi_{mn}^a (\Phi_{m'n'}^b)^* r dr \right\}. \quad (27)$$

From Eq. (27), LINFLUX calculates SPL by setting $\langle\langle\langle\tilde{a}\tilde{b}\rangle\rangle\rangle = \langle\langle\langle|\tilde{p}|^2\rangle\rangle\rangle$ and using the reference pressure of 2×10^{-5} Pa.

For the PWL calculations, the standard acoustic energy intensity formula, applicable to irrotational flows, is used. For ducted flows, this reduces to the axial component of acoustic energy intensity given by $I_\xi = (\bar{p}/\bar{\rho} + V_\xi \tilde{V}_\xi)(\bar{\rho}\tilde{v}_\xi + \tilde{\rho}V_\xi)$. LINFLUX computes PWL by setting $\langle\langle\langle\tilde{a}\tilde{b}\rangle\rangle\rangle = A_D \langle\langle\langle(\bar{p}/\bar{\rho} + V_\xi \tilde{V}_\xi)(\bar{\rho}\tilde{v}_\xi + \tilde{\rho}V_\xi)^*\rangle\rangle\rangle$ and using the reference power level of 10^{-12} watts.

Acoustic Calculations

As was indicated in the introduction, the interaction of the rotor wakes with the OGV is computed first. The rotor wake perturbations that drive the OGV acoustic response were extracted from a set of aerodynamic simulations for the ADP fan¹⁶. These simulations, which modeled the flowfields both inside and outside of the nacelle, were carried out at the five tip speed conditions highlighted in Table 2. The aerodynamic simulations were generated using an axisymmetric viscous flow solver called AVCS¹⁷ coupled to a three-dimensional viscous turbomachinery flow solver called TSWIFT¹⁷. These codes are based on similar algorithms, have multi-block capability, and solve the RANS-based flow equations on body-fitted grids using an explicit finite difference scheme. The simulations involved the entire fan system, therefore, only the fan rotational speed and fan stage pressure ratio were adjusted in order to set the fan operating point and ensure that the predicted mass flow rates matched the measurement values accurately. The codes output the distributions of the density, momenta and total energy variables. Figure 4 shows an example of the

^{§§} For plug flow base flows, these modal descriptions would reduce to the classical Bessel functions of the first and second kinds¹⁶, but for the sheared and swirling base flows they cannot be expressed in closed form and must be computed numerically¹⁷.

level of the fidelity of the CFD simulations. It shows the measured (using LDV) and CFD-based contours of the axial velocity at a location 4 inches downstream of the rotor stacking axis. The comparison is at the sideline operating condition. The left hand side of the figure shows the data and the right hand side shows the prediction. The contours are plotted on the same scale and over the same range. The LDV measurements did not extend to the duct wall regions in order to avoid laser beam reflections from the duct walls, but the simulations extend all the way to the duct walls. The gross features of the flowfield are captured quite well in the simulations and the levels are comparable too. In particular, the wake skewing (or titling), which strongly affects the spanwise phase of the incident wakes, is fairly well captured.

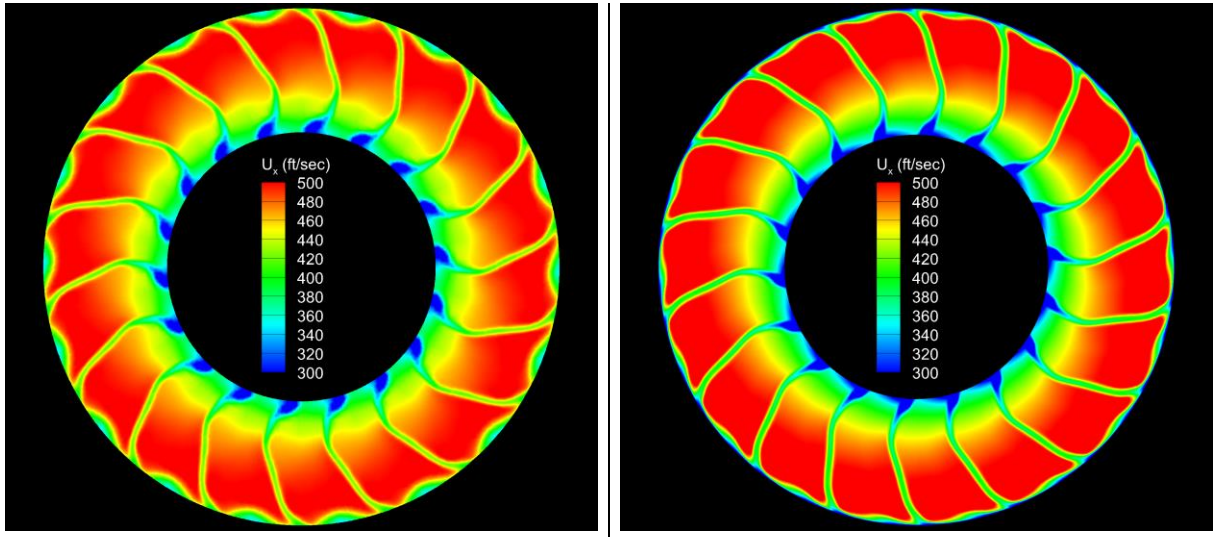


Figure 4. Contours of axial velocity for the ADP fan 4 inches downstream of the rotors stacking axis. LDV data are shown in the left column and the RANS prediction in the right column. Comparisons are shown for the sideline rpm for both fans.

For a more quantitative comparison, pitchwise profiles are extracted from the contour plots at the 25%, 50% and 75% spanwise locations and are compared in Figure 5. The pitchwise coordinate (expressed in degrees) is shifted so that the wake profiles are centered on the zero-degree location for easier comparison. Typically for these simulations, the RANS-based wakes are deeper (i.e., less diffused) than the measured ones with a maximum discrepancy of about 10%. The maximum discrepancy in the free stream velocity in the passage is less than 5% though in most cases the difference is significantly smaller. Owing to the physics of the R/S interaction problem, the BPF tone levels are linearly proportional to the harmonic content of the incident wakes. As such it is the discrepancies in the harmonic content of the measured versus predicted wakes that is the important measure of the fidelity. The wake depth discrepancy principally affects the BPF content of the wake, but since the BPF tone is cut-off for this fan, the difference is of no consequence for the purposes of this study.

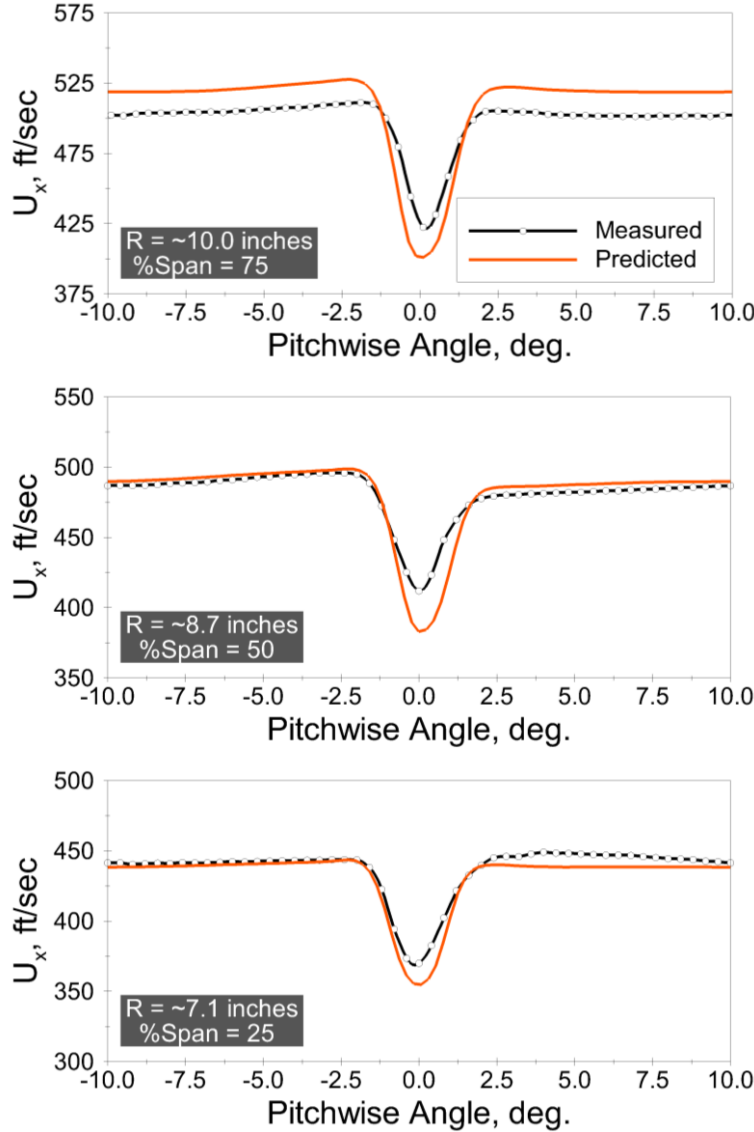


Figure 5. Comparisons of LDV and RANS pitchwise axial velocity profiles at three spanwise locations for the ADP fan.

The rotor wake input to the LINFLUX code is supplied in terms of the complex-valued Fourier amplitudes of the pitchwise wake profiles at a number of radial stations. The complex amplitudes are the coefficients in the Fourier decomposition of the pitchwise wake profiles in terms of the rotor blade passing frequency harmonics. The input for the companion TURBO code, which must be run first, requires the pitchwise-averaged profiles of total pressure, total temperature, and the swirl angle as a function of radius at the inflow plane. Both aerodynamic input sets have been extracted from the RANS simulations discussed earlier. As an example, Figure 6 shows a collage of these profiles for the ADP at the sideline condition (i.e., 8750 RPM). The wake harmonic contents shown in this figure are for the 2BPF component of the wake profile.

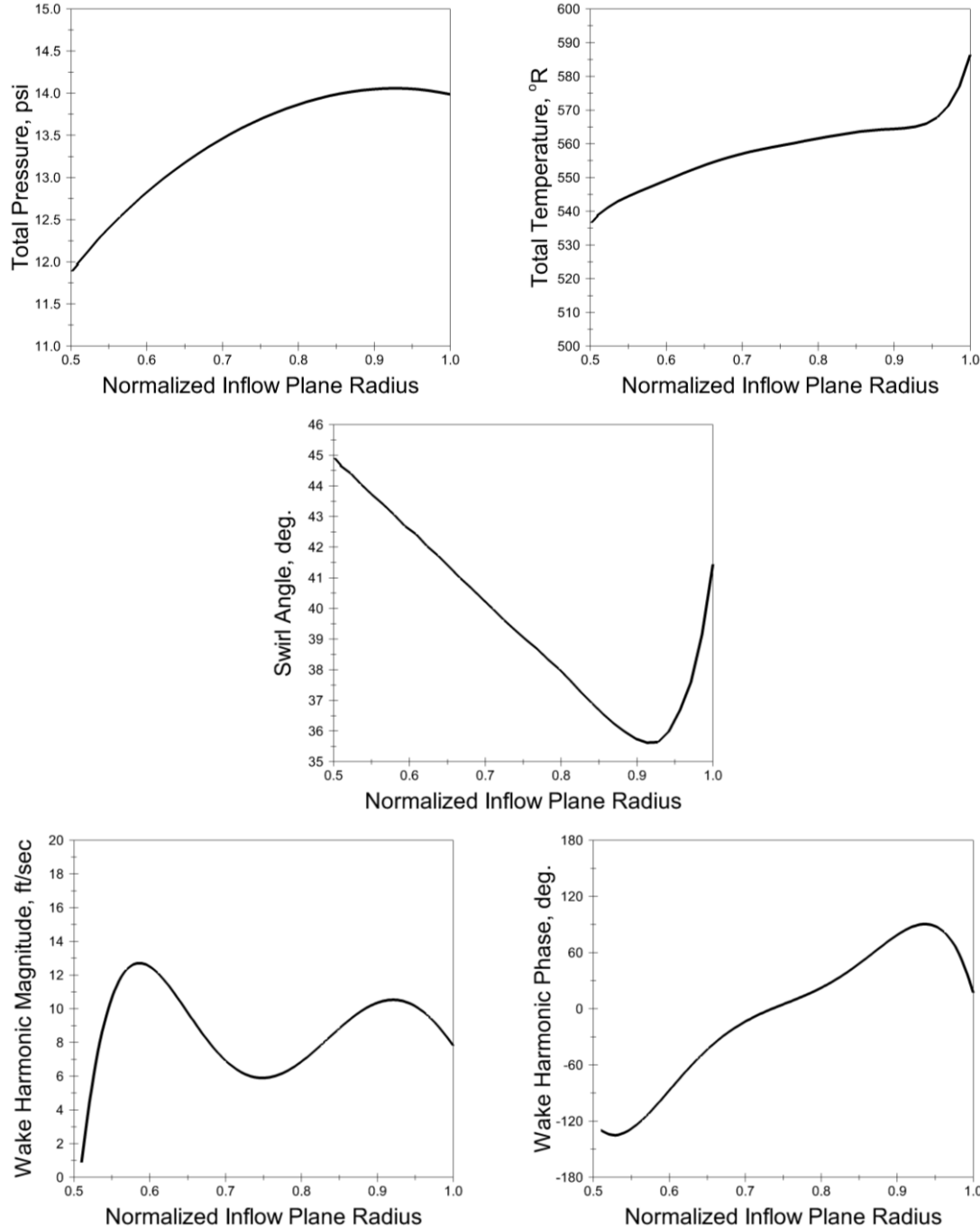


Figure 6. Typical spanwise profiles of steady flow parameters needed as input for the TURBO and LINFLUX calculations. The profiles shown are for the ADP fan operating at 8750-RPM speed condition.

The computational domain for the OGV calculations is shown in Figure 7. The domain, used for both TURBO and LINFLUX calculations, is a single three-dimensional grid block spanning one vane passage between the suction side of one vane and the pressure side of the adjacent vane. It extends axially roughly one vane chord upstream and

downstream of the vane passage. It is comprised of a stack of constant radii axial-circumferential layers from the hub to tip. It should be noted that, since both TURBO and LINFLUX are inviscid codes, the OGV's round trailing edge was modified and made sharp in order to avoid flow recirculation downstream of the trailing edge. The modification smoothly extended the OGV airfoil sections by about 6%. The axial \times circumferential \times radial dimensions of the OGV grid are $181 \times 43 \times 25$. The axial count guarantees minimum 40 grid points per wavelength at 2BPF since the acoustic wavelength is 2.4 inches (6.1 cm) at the highest RPM condition and the extended vane chord is approximately 1.7 in (4.2 cm). The circumferential count ensures that the target circumferential orders are well resolved. The radial count guarantees the smooth resolution of the expected radial mode shapes.

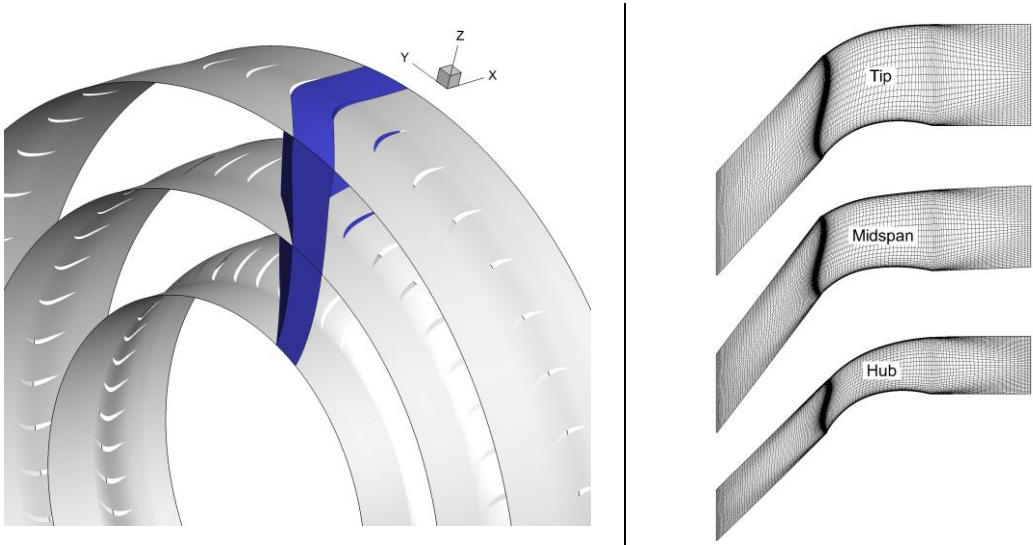


Figure 7. The computational domain used for the TURBO and LINFLUX computations of R/S interaction (left). It consists of a single passage between the suction side of one vane and the pressure side of the adjacent vane. Sample grid layers extracted from the domain at the hub, mid-span and tip are shown on the right.

An illustrative example of the field solutions computed by LINFLUX is shown in Figure 8 in which contours of the real part of the 2BPF perturbation pressure computed for the ADP fan are depicted. The top row shows the result for the approach condition (i.e., 5425 RPM) and the bottom row the results for the sideline condition (i.e., 8750 RPM). Contours of the propagating acoustic waves upstream and downstream of the OGV are plotted. At the approach condition, the upstream propagating acoustic field is composed of the three radial modes $(-9, 0)$, $(-9, 1)$ and $(-9, 2)$, and the downstream propagating acoustic pressure is composed of only $(-9, 0)$ and $(-9, 1)$ radial modes. At the takeoff condition, the upstream propagating acoustic field is comprised of the four radial modes $(-9, 0)$, $(-9, 1)$, $(-9, 2)$, and $(-9, 4)$ while the downstream propagating acoustic pressure is comprised of the radial modes $(-9, 0)$, $(-9, 1)$ and $(-9, 2)$. Here, consistent with the notation defined earlier, we use the notation (m, n) to identify a radial mode n belonging to the circumferential mode set m . All other computed modes are predicted by LINFLUX to be evanescent. It is possible to discern the circumferential lobe pattern, i.e., the circumferential mode index (which is 9

in this case), by counting the number of interlaced positive/negative peaks (i.e., the red and blue regions) in the contours of the upstream and downstream pressure or the pressure traces on the duct walls. Note the negative sign on the index m signifies the fact that mode is counter-rotating to the rotor.

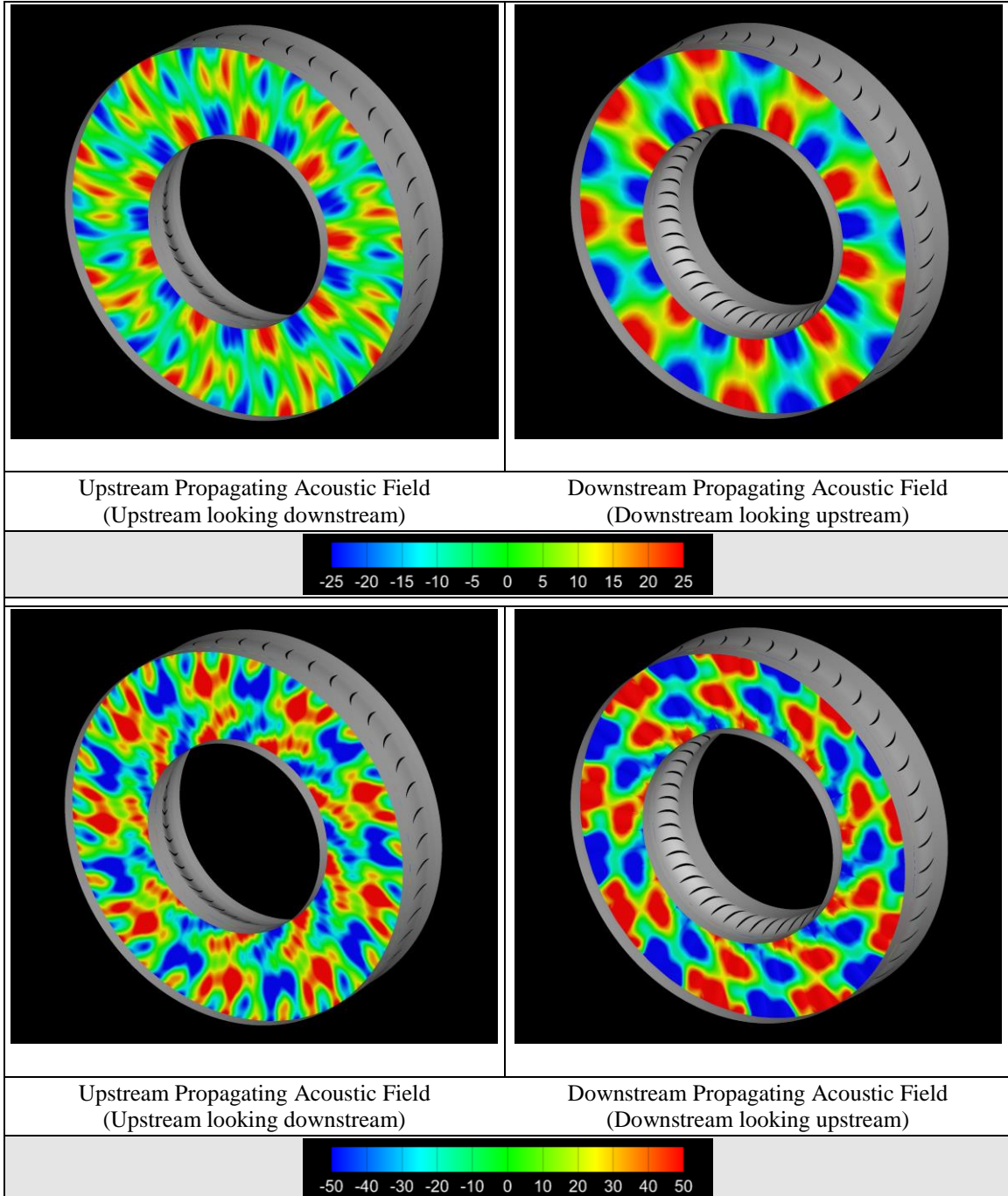


Figure 8. Contour plots of predicted real part of the 2BPF perturbation pressure (in Pa) generated by the R/S interaction for the ADP fan at the approach condition (top row) and the sideline condition (bottom row). Propagating circumferential mode ($m = -9$) is plotted in all cases.

LINFLUX computations for the rotor wake impinging on the OGV were carried out for all of the tip speeds listed in Table 2. For tip speeds, for which CFD simulations did not exist, the steady flow TURBO input parameters and LINFLUX input wake harmonics (see Figure 6) were interpolated or extrapolated from the profiles available for the five tips speeds for which CFD simulations did exist. This was considered justified since the profiles vary fairly monotonically with the fan rotational speed. The predicted SPL and PWL are shown on a mode-by-mode basis for both the upstream and downstream propagating modes in Figures 9 and 10. A few trends are discernible in the results. For the most part, the downstream propagating modes have higher SPL and PWL than the corresponding modes ones at the same tip speed (note the scale difference between the upstream and downstream plots). As the fan rotational speed increases so do the number of propagating radial modes and, usually, their SPL and PWL as well. Also, with some exceptions, the SPL and PWL tend to decrease with the increasing radial mode order at a given fan speed.

Unfortunately, there are no direct in-duct measurements of the modal SPL and PWL to which these predictions can be directly compared on a mode-by-mode basis ***. However, it is possible to compare the predicted in-duct tone power levels to the external tone power levels obtained from the tunnel measurements on the basis of the total power in the 2BPF tone. For this purpose, the LINFLUX modal power level for the 2BPF tone are summed and compared with the 2BPF tone power levels computed from the sideline microphone measurements described in the experimental data section. Figure 11 shows the comparison of the predicted PWL upstream and downstream of the OGV to the measured PWL levels in the inlet (solid symbols) and the exhaust (open symbols) as a function of fan RPM. There are three sets of wind tunnel measurements obtained for the ADP fan over the years and they are all plotted to provide a measure of repeatability of the data for the same hardware operating at the same conditions. The uncertainty in the measurements of SPL, and hence in PWL, is ± 1 dB. The predictions are shown with a left open triangle for the upstream level and a right open triangle for the downstream level. For a better appreciation of the trends in the predicted levels, trend lines have been fitted to the predictions; the solid line for the upstream PWL and the dashed line for the downstream PWL.

Since there is no hardware downstream of the OGV, it is legitimate to compare the predicted in-duct PWL downstream of the OGV with the measured exhaust power level. The predicted 2BPF acoustic power levels downstream OGV match the measured 2BPF exhaust power levels quite well (i.e., to within the experimental scatter and measurement uncertainty) across the speed range. In contrast, the predicted PWL upstream of the OGV cannot justifiably be compared with the measured inlet PWL since the effect of the rotor acoustic transmission is not been taken into account in these predictions. Nevertheless, the comparisons serve to provide an estimate of the level rotor acoustic transmission loss due to the presence of the rotor. It is clear from Figure 12, which shows the ADP fan stage form directly upstream, that the rotor transmission loss levels implied by Figure 11, cannot simply be the result of geometric blockage by the rotor blades (often called the venetian blind effect) given the relatively open fan blade passage. Rather, they must be a result of

*** Mode SPL and PWL acquired using the rotating rake (RR) data system¹² cannot be reliably used for comparison purposes since the RR data reduction system parses the measured acoustic pressure in terms of classical duct modes and not the more representative swirl or shear flow duct modes that are computed by LINFLUX.

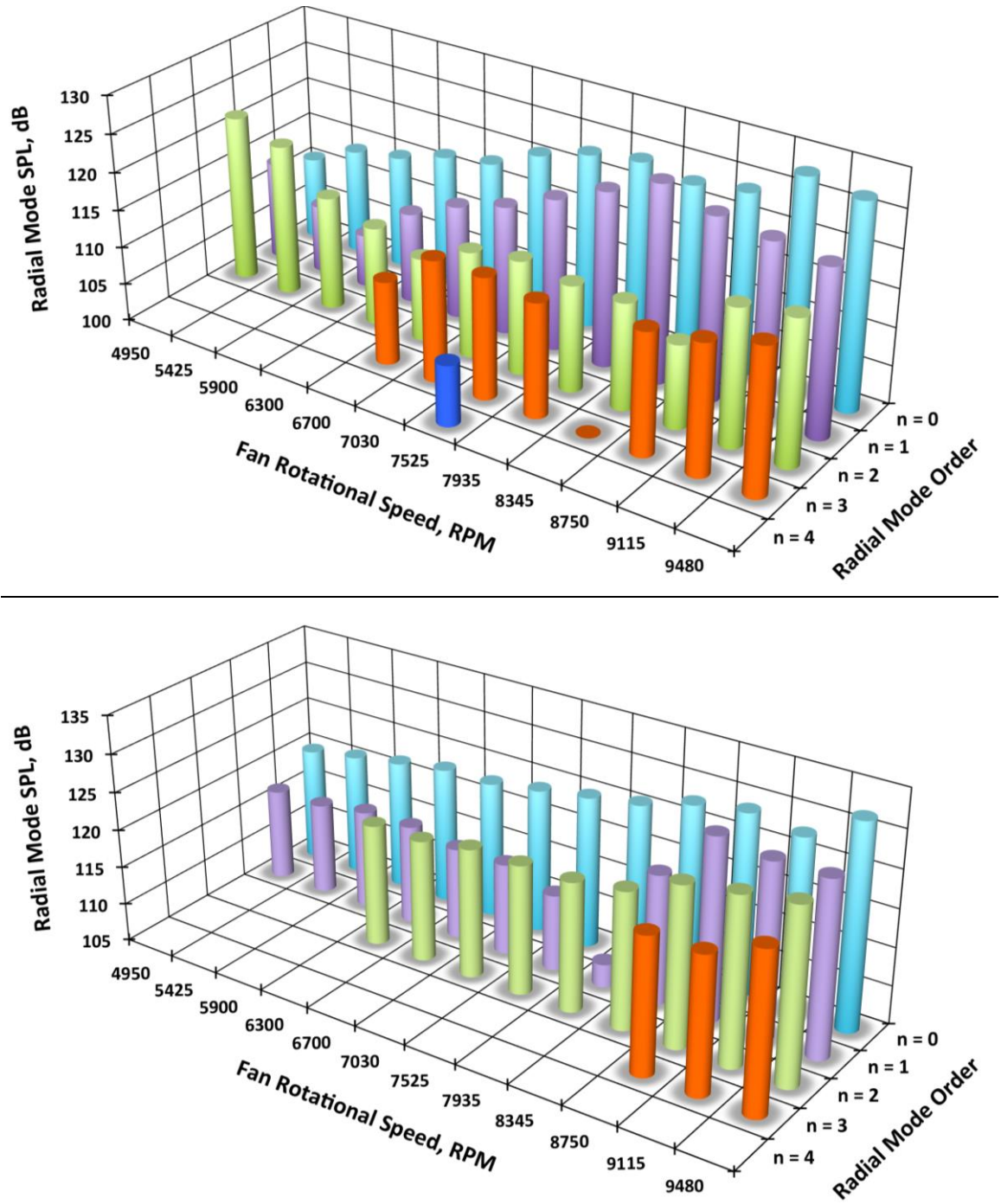


Figure 9. Predicted SPL distribution for the propagating radial modes in the circumferential mode $m = -9$ produced as a result of the rotor wake impingement on the OGV. Upstream propagating mode levels are shown on the top and the downstream levels on the bottom. Frequency is 2BPF.

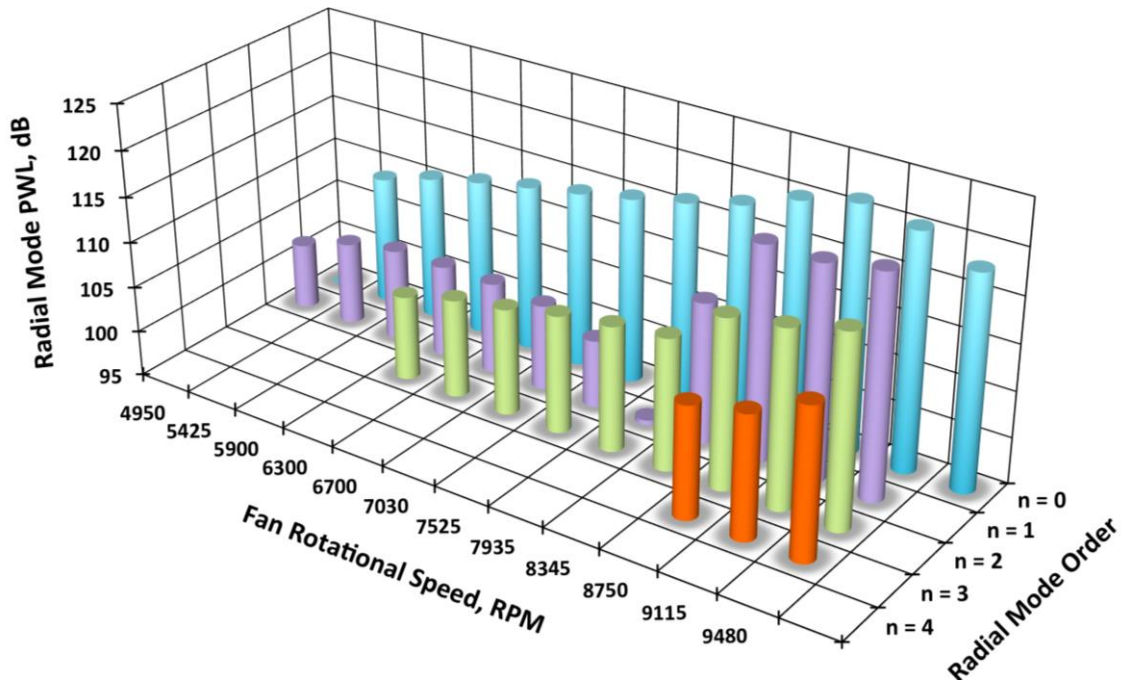
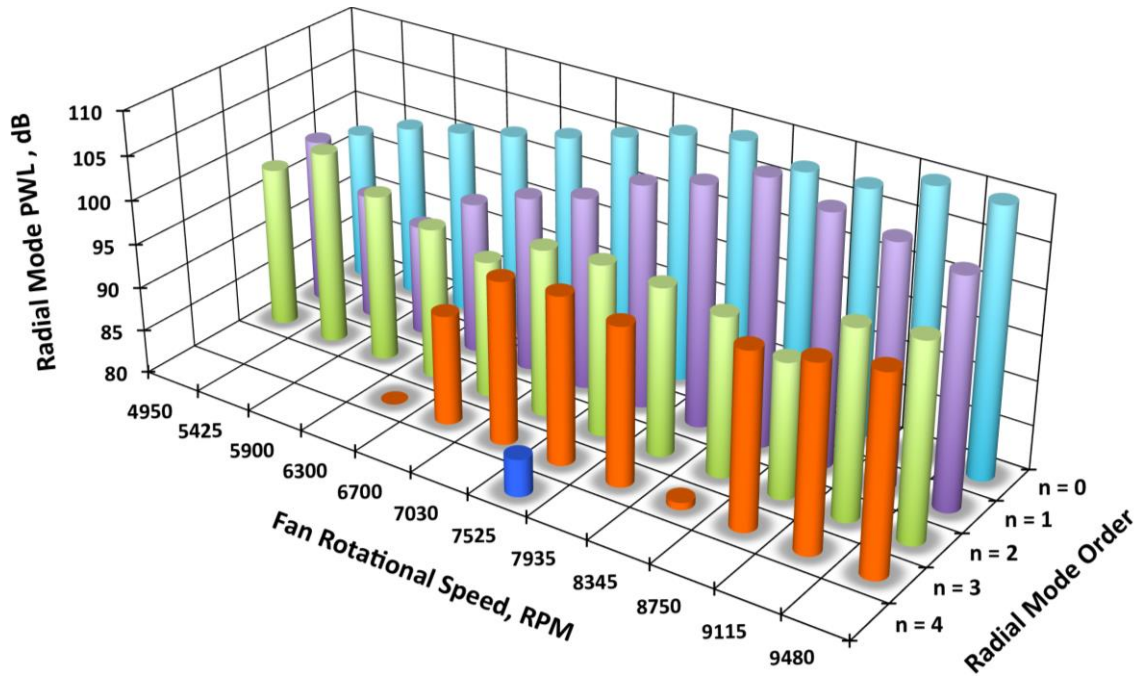


Figure 10. Predicted PWL distribution for the propagating radial modes in the circumferential mode $m = -9$ produced as a result of the rotor wake impingement on the OGV. Upstream propagating mode levels are shown on the top and the downstream levels on the bottom. Frequency is 2BPF.

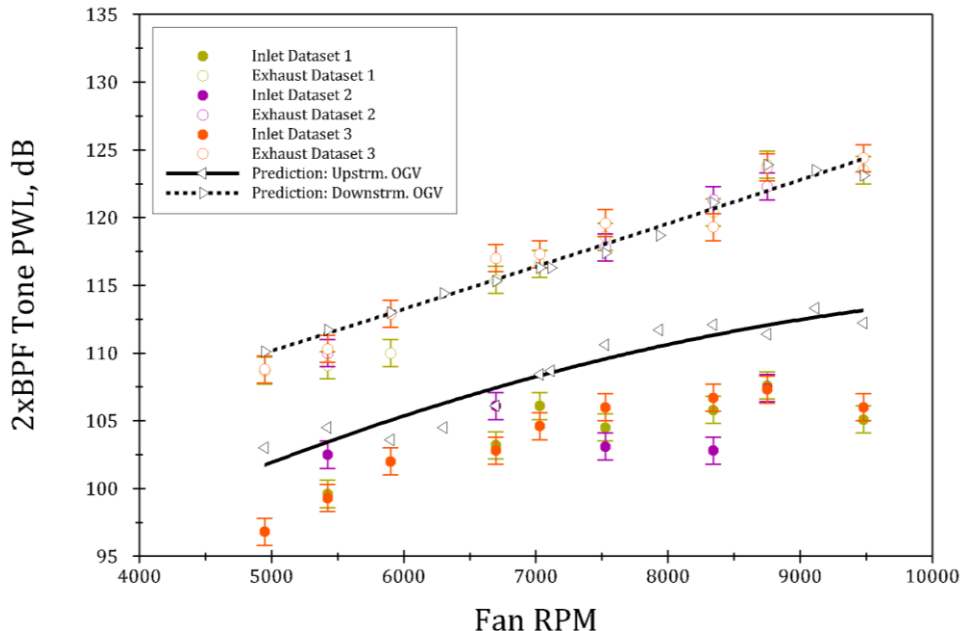


Figure 11. Comparisons of measured and predicted 2BPF tone power levels for the ADP fan as a function fan RPM. The power levels are a result of the rotor wake interacting with the OGV. The OGV upstream levels (left triangles) and downstream levels (right triangles) are plotted. The solid and dashed lines are trend lines fitted to the predicted levels. The experimental data (three sets) show the acoustic power levels outside of the fan duct calculated using the sideline acoustic levels measured in the wind tunnel. The solid symbols denote the levels for the inlet and open symbols those for the exhaust levels. The effect of rotor transmission on the upstream OGV upstream levels is not included.

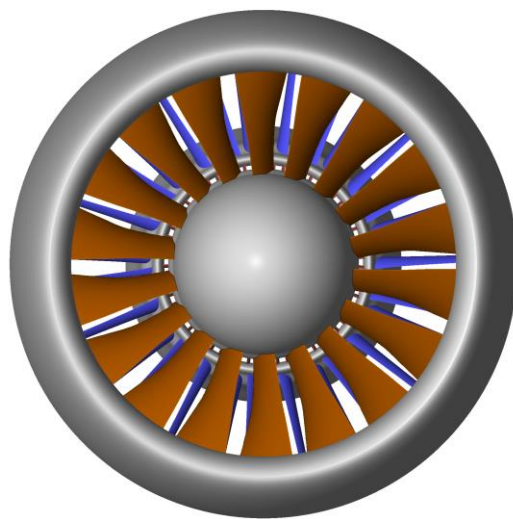


Figure 12. Front view of the ADP fan stage (upstream looking downstream).

the flow blockage and scattering of the incident sound field by the rotating fan blades. With the modal distribution of the OGV upstream propagating acoustic field computed in the previous step, we proceed to use LINFLUX to compute the response of the rotor to these incident acoustic disturbances.

The analysis follows similar lines to the OGV response calculations except that the input excitations in this case are not from incident wakes of an upstream blade row, but from upstream propagating acoustic disturbances imposed at the outflow plane of the rotor computational domain. The computational domain for the rotor is topologically similar to that shown in Figure 7 for the OGV, but it is proportionally denser in all three directions in order to accommodate the larger axial extent^{†††}, the lower hub-to-tip radius ratio, and lower airfoil count. With these considerations axial \times circumferential \times radial dimensions of the rotor grid were set at $281 \times 107 \times 35$. TURBO calculations were carried out for all speed conditions considered in this study using the rotating frame total pressure, total temperature and swirl angle (*add a figure?*). With the relative frame mean flows computed, LINFLUX was run to compute the response of the rotor to the incident OGV upstream propagating acoustic field.

Since, LINFLUX compute the blade row response in a coordinate system fixed to the target blade row, the rotor response calculations were carried out in the rotating frame. As such the input acoustic disturbances must be appropriately represented in the rotating frame. For small amplitude acoustic disturbances of interest here, the only change required is to switch from a tangential coordinate θ_s in the stationary frame to tangential coordinate θ_r in the rotating frame via $\theta_s = \theta_r + \Omega t$ where Ω is the rotor rotational speed. Therefore, the circumferential-temporal phase of a 2BPF (i.e., $2B\Omega = 36\Omega$) harmonic acoustic disturbance,

$$p'_{mn}(r, \theta_s, \xi, t) = a_{mn} \Phi_{mn}(r) e^{\chi_{mn}\xi} e^{i(m\theta_s + 36\Omega t)}, \quad (28)$$

in the stationary frame of reference is transformed, in the rotating frame of reference to

$$\text{Incident Phase: } \underbrace{m\theta_s + 36\Omega t}_{\text{stationary frame}} = \underbrace{m(\theta_r + \Omega t) + 36\Omega t}_{\text{rotating frame}} = m\theta_r + (36 + m)\Omega t. \quad (29)$$

Therefore, in the rotating frame, the 2BPF disturbance will have a shifted frequency commensurate with its circumferential order, but it will retain its circumferential order identity. However, the interaction with the rotor blade row is expected to generate additional circumferential mode orders. The general form of the circumferential-temporal phase of the scattered field has the form

$$\text{Scattered Phase: } \underbrace{(m + kB)\theta_r + (36 + m)\Omega t}_{\text{rotating frame}}, \quad (30)$$

^{†††} As pointed out earlier the axial extent of the domain is roughly three airfoil axial chords. The stator vane chord is 1.7 inches (4.2 cm) and the rotor blade chord is 3.7 inches (9.4 cm). Taking into account the average stagger of the two blade rows, the rotor domain is roughly 1.7 longer in the axial direction. The 281 axial grid points was a slight compromise to keep the grid size relatively modest.

where k is the circumferential mode scattering index^{†††}. Transforming back to the stationary frame, the scattered field will have the form

$$\text{Scattered Phase: } \underbrace{(m+kB)(\theta_s - \Omega t) + (36+m)\Omega t}_{\text{stationary frame}} = (m+kB)\theta_s + (36-kB)\Omega t, \quad (31)$$

indicating that, when viewed in the fixed frame of reference, the rotor scatters an incident wave of a given circumferential more order into a family of circumferential mode orders whose frequencies are shifted. Therefore, if the incident circumferential mode is $m = -9$, the incident and scattered waves have the forms

$$\text{Scattered Phase: } \underbrace{(-9+18k)\theta_s + (36-18k)\Omega t}_{\text{stationary frame}}. \quad (31)$$

Recall that the rotor blade count is 18. As a result, the scattered acoustic field expressed in the stationary frame of reference has the form,

$$p'_{(-9+18k)n'}(r, \theta_s, \xi, t) = a_{(-9+18B)n'} \Phi_{(-9+18k)n'}(r) e^{\chi_{(-9+18k)n'} \xi} e^{i[(-9+18k)\theta_s + (36-18k)\Omega t]}. \quad (32)$$

Therefore, the LINFLUX solutions for the rotor response calculations must be filtered so as to isolated the 2BPF tone contribution and exclude the contribution of the other tones, i.e., scattered waves with shifted frequencies.

It should be pointed out that, theoretically, other tone harmonics, i.e., $j \times \text{BPF}$ tones ($j = 1, 3, 4$, etc.) can conceivably produce a 2BPF response due to rotor scattering. However, as can be seen in Figure 13, which shows the computed OGV response at BPF compared with that for 2BPF, that the BPF tone is strongly evanescent and is not likely to produce a significant scattered field at 2BPF due to interaction with the rotor. Furthermore, experimental data indicates that tones higher than 3BPF are rather weak and typically at or below the broadband level and again are unlikely to produce sizable 2BPF response due to rotor scattering. Therefore, the only likely candidate for additional 2BPF contribution due to rotor scattering is the 3BPF tone. The inclusion of the 3BPF tone would have required commensurately denser grids in the OGV calculations. It also would have required, much denser grid for the rotor calculation, since the shifted frequency of the primary circumferential mode in the 3BPF tone (which turns out to be $m = +9$) is 63Ω ; i.e., Eq. (30) for the 3BPF incident wave has the form $(9+kB)\theta_r + (54+9)\Omega t$. An analysis of the eigenvalue problem for the 3BPF incident wave on the rotor suggests that the primary scattered modes result in evanescent modes, but this conclusion is not rigorous in that the existing rotor grid was used which may not be sufficiently resolved for the task. In any case, a detailed assessment of the contribution of the 3BPF tone is beyond the scope of the present effort and will be addressed in a future investigation.

^{†††} In general, the scattering process also generated radial modes other than the indent one whether the interaction is with a rotor or a stator. More will be said about this aspect of the interaction later in the paper.

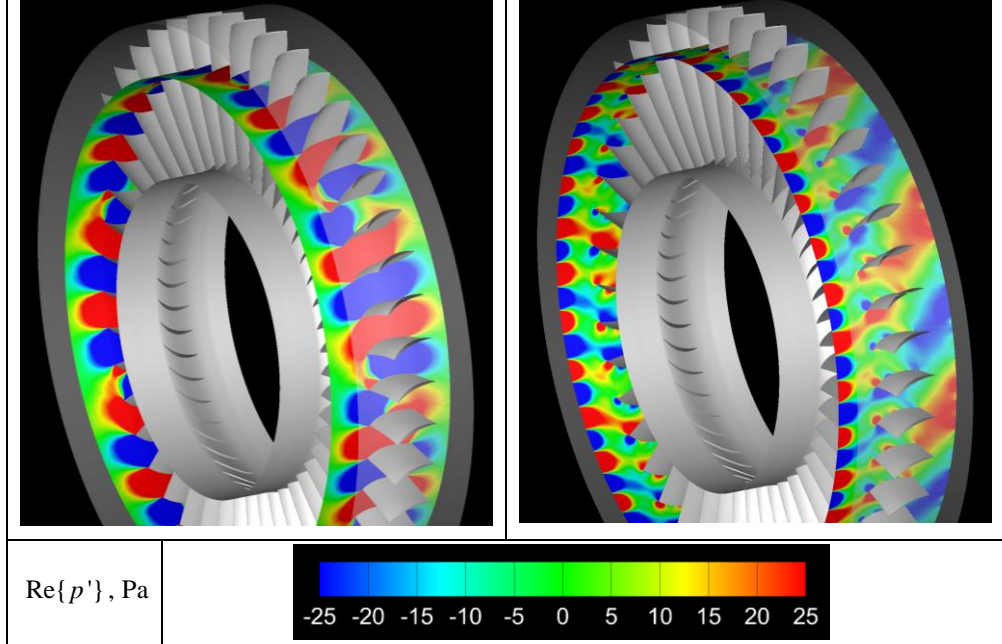


Figure 13. Contour plots of real part of the perturbation pressure generated by the R/S interaction for the ADP fan at the approach conditions (i.e., 5425 rpm). Levels at 75% span are plotted. Shown on the left are the pressure contours for the BPF tone and on the right those for the 2BPF tone. Due to ADP's "cut-off" blade/vane count ratio, the BPF tone is cut-off (i.e., it is evanescent) for this fan. By contrast the 2BPF tone is cut-on (i.e., propagating).

While the LINFLUX computations for the first 10 fan tip speeds converged normally, those for the highest two speeds, namely, 9115 RPM and 9480 RPM, did not. Comparisons of the TURBO flowfields for these two tip speeds with those from the lower RPM cases did not reveal any obvious issues. However, the current hypothesis is that the presence of small pockets of supersonic flow on the blade near the leading edge may be responsible for the instability of the perturbation solution in LINFLUX. The TURBO solutions at lower tip speeds do not exhibit such supersonic bubbles. It may be possible that by fine-tuning the input swirl angle profiles, or total pressure profiles, in the TURBO input decks, these pockets could be eliminated. However, for this study, no attempt was made to tweak these parameters and instead the LINFLUX predictions for these two cases are missing from the results to be presented next.

We begin the presentation of the result with the computed scattered modal SPL and PWL distributions. In the LINFLUX calculations, the response was restricted to $k \in (-1,0,1)$, since preliminary calculations indicated that for $|k| > 1$ all modes were predicted to be evanescent. As a result, the scattered circumferential modes computed by LINFLUX belong to the subset $m_{\text{scattered}} \in (-27, -9, 9)$ whose corresponding frequencies in the stationary frame of reference are $\omega_{\text{scattered}} \in (54\Omega, 36\Omega, 18\Omega) = (3\text{BPF}, 2\text{BPF}, \text{BPF})$. Note that the circumferential order of the scattered acoustic field that has the frequency 2BPF has a circumferential mode order of -9. The other circumferential modes have

frequencies BPF and 3BPF. Since the focus here is on the 2BPF tone response, in the interest of brevity, the other modes are not included in the results presented here.

The SPL and PWL levels for the scattered circumferential mode $m_{\text{scattered}} = -9$ are plotted in Figure 14 on the basis of its radial mode content. These distributions are for modes that are predicted to propagate upstream of the rotor. Technically these modes represent the transmitted portion of the incident $m_{\text{incident}} = -9$ mode that was generated by the OGV in response to the incident wakes of the rotor at 2BPF and discussed earlier in the paper. A comparison of the modal sound pressure and power levels shown in the top halves of Figures 9 and 10 with those in Figure 14 clearly show that both modal pressure and power levels have been affected by the encounter with the rotor and for the most part both have suffered some transmission loss. The only relatively obvious pattern in these results is that the higher order radial modes tend to have been effected more dramatically by the transmission through the rotor than the lower order ones. Otherwise, the transmission loss does not seem to have a clear and definable pattern with speed for a given mode order.

It should be noted here that the levels shown in Figure 14 represent sums of pressure and power levels for a given mode that are aggregates of levels for the same mode produced by all of the incident radial modes. Put differently, each incident radial mode n_{incident} gives rise, through the scattering process, to a distribution of propagating and evanescent radial modes $n_{\text{scattered}}$. Thus, for example, the incident radial mode $n_{\text{incident}} = 0$ gives rise to the scattered set of radial modes $n_{\text{scattered}} \in (0, 1, 2, \dots)$ as does the incident mode $n_{\text{incident}} = 1$, and the incident mode $n_{\text{incident}} = 2$, etc. As such, the SPL and PWL of a given scattered radial mode plotted in Figure 14 represents the sum of all pressure and power levels for that radial mode generated by all the incident radial modes. It should also be noted that the SPL level for each scattered radial mode is the dB level for the complex sum of the linear mode amplitudes produced by all the incident radial modes. The PWL is, on the other hand, summed antilogarithmically, since the phase does not play role in the summing process.

A sample plot of the radial mode scattering phenomenon is shown in Figure 15 for one fan speed (namely, 7525) and is representative of the essence of the process for all other speeds. As can be seen in the figure, every incident radial mode gives rise to all propagating radial modes in the scattered field. The importance of the radial mode scattering process cannot be over-stated. In most analytical models of blade row acoustic transmission loss, there is no mechanism for radial mode scattering. This is often because the underlying mathematical problem is assumed two-dimensional in the ξ and θ coordinates and the dependence on the radial coordinate r is ignored. As such, the estimate of transmission loss from such models be higher than warranted because each radial mode scatters only into itself and not into other possible propagating modes. Therefore, if the resulting scattered mode is predicted to have low power or be cut-off, then the portion of the energy in the incident radial mode that would have scattered into other radial modes is also ignored thus estimating higher levels of transmission loss than warranted. Clearly, an accurate treatment of the problem requires a three-dimensional analysis (be it analytical or numerical) in order to account for the radial mode scattering phenomenon.

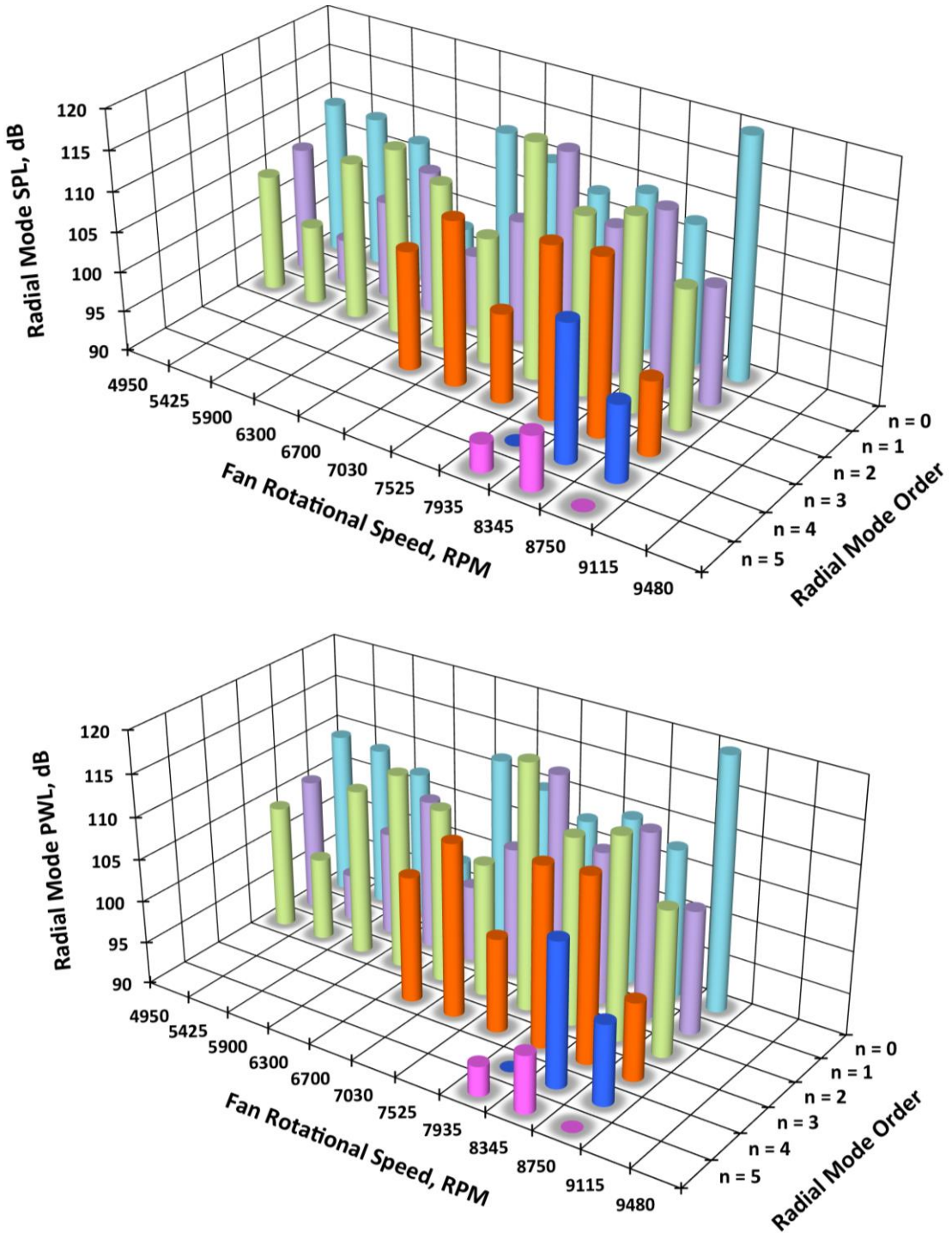


Figure 14. Predicted modal SPL and PWL distributions for the propagating radial modes in the scattered circumferential mode $m = -9$ propagating upstream of the rotor. SPL distribution is shown on the top and the PWL distribution on the bottom. Frequency is 2BPF.

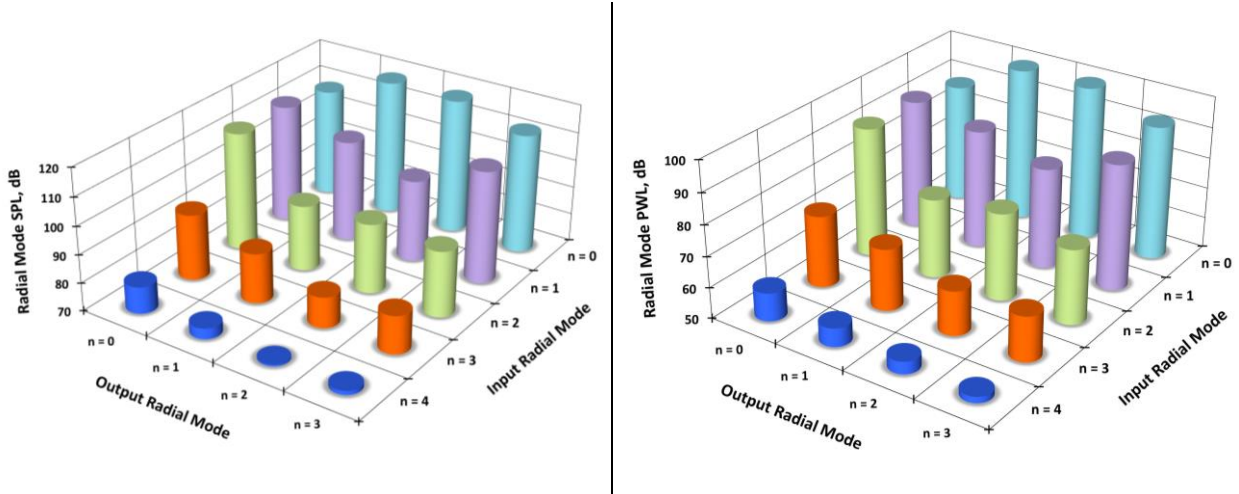


Figure 15. Predicted radial mode scattering for the 7525 tips peed condition. SPL distribution is shown on the left and the PWL distribution on the right. Each input radial mode is scattered to every propagating radial mode. Frequency is 2BPF.

It should be noted that the downstream SPL and PWL modal distribution, i.e., the counterparts to those in Figure 14 are difficult to compute. That is because, whereas the idea of an evanescent mode upstream of the rotor or downstream of the OGV is fairly clear and intuitive, this is not so in the region between the rotor and OGV. As the waves generated upstream of the OGV due to the wake impingement propagate towards the rotor, they undergo a process of evolution and their amplitudes and wavenumbers continually change subject to the variations in the mean flow. Acoustic waves that start as propagating in the vicinity of the OGV may become evanescent as they approach the rotor or vice versa. This effect is approximately accounted for in the results presented here as follows. Since the eigenvalue problem associated with the outflow plane of the rotor domain is different from the eigenvalue problem associated with the inflow plane of the OGV domain, the wavenumbers of the propagating and evanescent radial modes at the two plane differ consistent with the changes in the mean flow for the two domain. However, since the radial mode order index is consistent between the two domains for the same circumferential mode order, as an approximation, the complex amplitudes of the predicted outgoing modes at the inflow of the OGV domain were assigned as the in-going mode amplitudes at the outflow plane of the rotor domain. As such, LINFLUX assigns the wavenumbers of these input radial modes according to the eigenvalue associated with the rotor. Therefore, the input radial modes have a discontinuous, rather than a smooth transition from the old values (those at the OGV domain's inflow plane) to the new values (those at the rotor domain's outflow plane). Otherwise, the problem would be intractable if it were solved one blade row at a time, as was done here.

Returning to the question of the predicted modal SPL and PWL distribution downstream of the rotor, LINFLUX calculates only SPL and PWL for the propagating modes at the rotor domain's outflow plane. In reality a fair amount of energy may be associated with the evanescent modes in that region that could undergo transition to propagating modes as they travel through a region where the mean flow changes continuously and/or they interact with the OGV. As such the SPL and PWL distributions

for the rotor outflow plane would represent only a subset of the acoustic energy in the inter-stage region. In fact, LINFLUX predicts a large number of evanescent modes at the rotor domain's outflow plane. However, in the interest of completeness, the distribution of the propagating modes is plotted in Figure 16. The number of propagating modes is relatively small which is an indication that the reflect energy from the rotor ends up in mostly a decaying field. But, this energy budget is available for transformation propagating modes either through the mean flow effects or through scattering by the stator. The only obvious pattern in the result of Figure 16 is that there is more propagating enraging in the higher RPM conditions than the lower ones.

Finally, since the modal power level distribution upstream of the rotor has been computed, one can sum the modal power at each speed to estimate the acoustic power level in the inlet. This is done and the results are plotted in Figure 17. The layout and most of the detail of the figure are exactly the same as those in Figure 11, but in this figure, the predicted acoustic PWL in propagating modes upstream of the rotor are also plotted. To emphasize the new results and avoid confusion, the predicted PWL upstream of the OGV are shown in a light gray color and the PWL upstream of the rotor are shown in black. The PWL downstream of the OGV is the same as that in Figure 11.

The levels upstream of the rotor, while under-estimating the measured inlet power levels somewhat, are more representative of the inlet levels compared with the levels upstream of the OGV (i.e., without rotor transmission loss) for two reasons. First, the trend of the inlet power level variation with speed is more accurately represented by the new levels compared with the more monotonic trend in the OGV upstream levels. Second, as was alluded to in the experimental section of the paper, the measured levels in the inlet include not only the contribution from the $m = -9$ circumferential mode at 2BPF, but also other extraneous circumferential modes produced at the 2BPF frequency due to imperfections in the manufacture and installation of the individual blades and vanes. The computational aerodynamic and aeroacoustic models and codes used in this work (i.e., RANS CFD, TURBO and LINFLUX) all assume perfectly identical airfoils in each blade row and thus cannot generate circumferential order other than those dictated by the Tyler-Sofrin rule. As such, the predicted level would inherently under-estimate the acoustic pressure and power levels of the real hardware to some extent. Additionally, as was discussed earlier in the results section, there is some possibility that the 3BPF tone generated as result of R/S interaction when scattered by the rotor could, potentially, produce non-negligible scattered field in the 2BPF frequency. Of course, there is also potential for other source mechanisms that have not been accounted for, such as the ever-present decaying rotor-locked static pressure field variation that could scatter into propagating modes due to the flow impedance change at the inlet highlight. That field has BPF harmonic content.

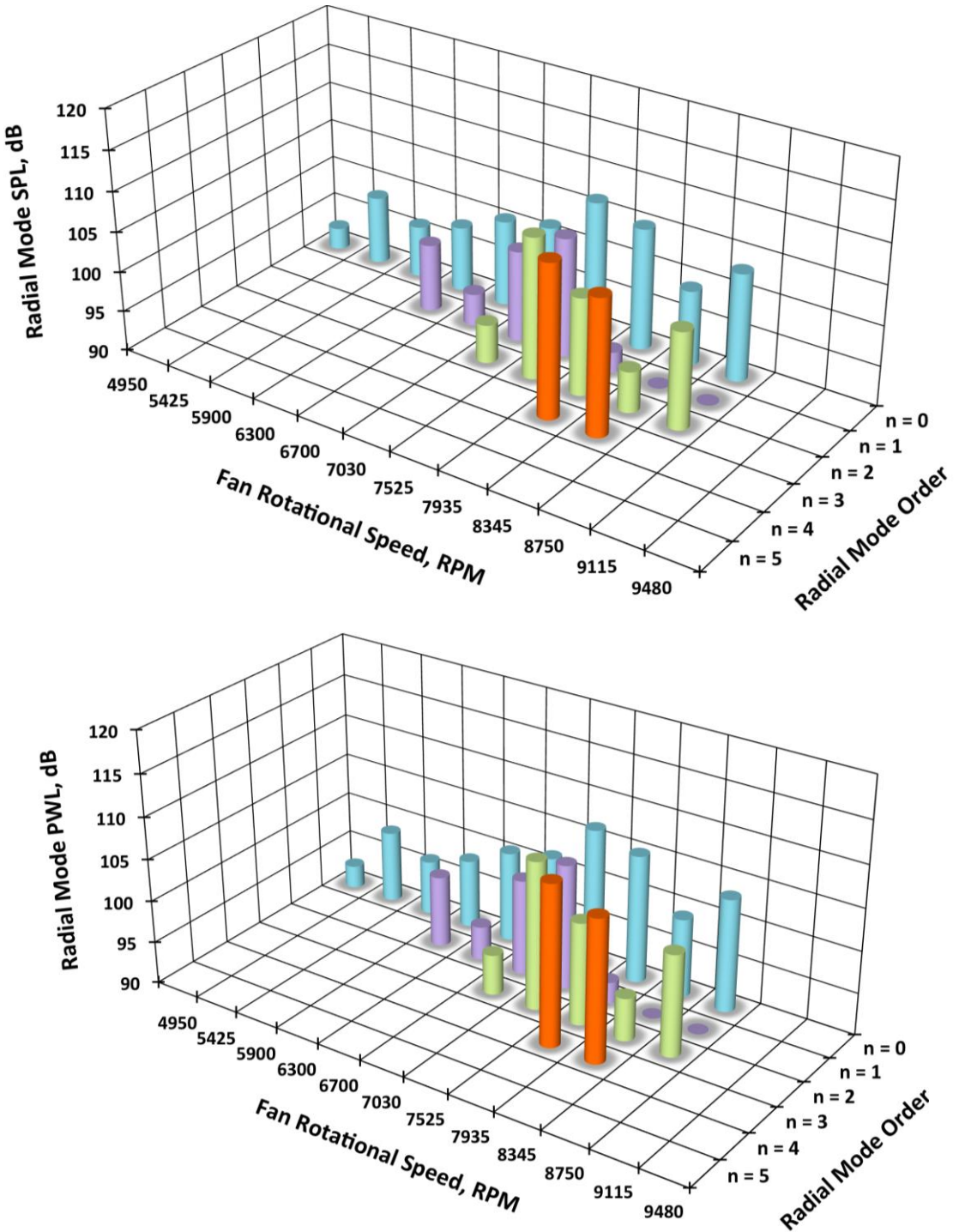


Figure 16. Predicted modal SPL and PWL distributions for the propagating radial modes in the scattered circumferential mode $m = -9$ propagating downstream of the rotor. SPL distribution is shown on the top and the PWL distribution on the bottom. Frequency is 2BPF.

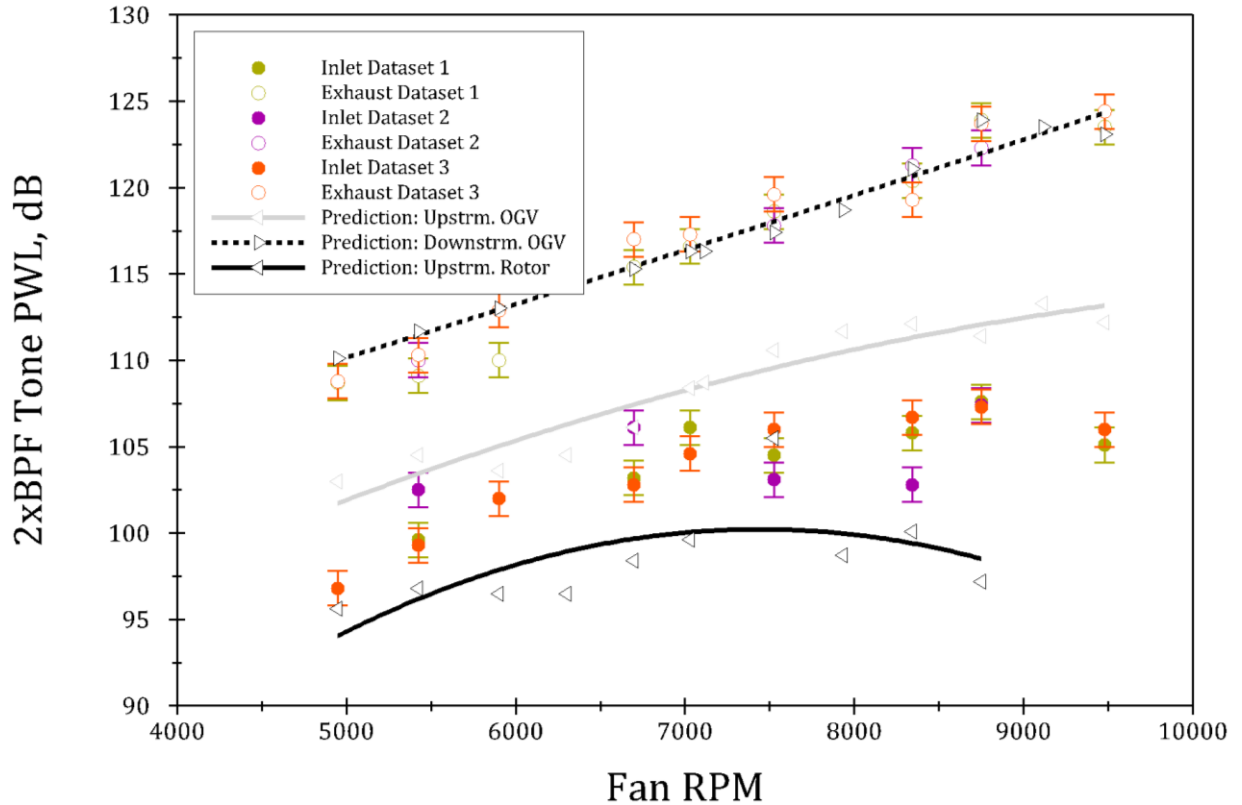


Figure 17. Comparisons of measured and predicted 2BPF tone power levels for the ADP fan. Predictions are for the OGV in-duct acoustic power levels without the effect of rotor transmission included. The levels upstream of the OGV (left triangles) and downstream of OGV (right triangles) are plotted. The solid and dashed lines are trend lines fitted to the predicted levels. The experimental data (three sets) show the acoustic power levels outside of the fan duct calculated using the sideline acoustic levels measured in the wind tunnel. The solid symbols denote the levels for the inlet and open symbols those for the exhaust levels.

Summary

To be added.

Acknowledgement

This work was supported by the NASA Advanced Air Transportation Technology (AATT) Project.

References

1. Mani, R. and Horvay, G., "Sound Transmission Through Blade Rows," *Journal of Sound and Vibration*, Vol. 12, no. 1, 1970, pp. 59-83.
2. Amiet, R.K., "Transmission and Reflection of Sound by Two Blade Rows," *Journal of Sound and Vibration*, Vol. 34, no. 3, 1970, pp. 399-412.
3. Hanson, D.B., "Acoustic Reflection and Transmission of 2-Dimensional Rotors and Stators, Including Mode and Frequency Scattering Effects," NASA Contractor Report NASA/CR-1999-208880, March 1999.
4. Hixon, D.R., Envia, E., Dahl, M.D., and Sutliff, D.L., "Comparison of Computational Aeroacoustics Prediction od Acoustic Transmission Through a Three Dimensional Stator Geometry with Experiment," Paper AIAA 2014-1405, 52nd Aerospace Sciences Meeting, January 13-17, 2014.
5. Logue M.M. and Atassi, H.M., "Scattering of Acoustic Waves by a Rotor," AIAA Paper 2008-2989, 14th AIAA/CEAS Aeroacoustics Conference, May 2008, Vancouver, Canada.
6. Mincu, D.-C., Polacsek, C., Manoha, E., and Clair, V., "Acoustic Transmission Through a 3D Rotating Fan Using Computational AeroAcoustics," 18th AIAA/CEAS Aeroacoustics Conference, June 2012, Vol. 50, no. 4, 1977, pp. 479-508.
7. Montgomery, M.D. and Verdon, J.M., "A Linearized Unsteady Euler Analysis for the Turbomachinery Blade Rows Using an Implicit Wave-Split Scheme," *Unsteady Aerodynamics and Aeroelasticity of Turbomachines*, edit by Y. Tanida and M. Namba, Elsvier, Amsterdam, pp. 143-160, 1995.
8. Montgomery, M.D. and Verdon, J.M., "A 3D Linearized Euler Analysis for Turbomachinery Blade Rows, Part 1: Aerodynamic and Numerical Formulations; Part 2: Unsteady Aerodynamic Response Predictions, Unsteady Aerodynamics and Aeroelasticity of Turbomachines," edit by T.H. Fransson, Kluwer Academic Publishers, pp. 427-464, 1998.
9. Verdon, J.M., "Linearized Unsteady Aerodynamic Analysis of the Acoustic Response to Wake/Blade-Row Interaction," NASA/CR-2001-210713, January 2001.
10. Dahl, M.D., and Woodward, R.P., "Acoustic Evaluation of the NASA Lewis 9- by 15-Foot Low-Speed Wind Tunnel," NASA TP-3274, 1992.
11. Tyler, J.M. and Sofrin, T.G., "Axial Flow Compressor Noise studies," *SAE Transactions*, Vol. 70, 1962, pp. 308-332.

12. Sutliff, D.L., "Turbofan Duct Mode Measurements Using a Continuously Rotating Microphone Rake," Int. J. Aeroacoustics, Vol. 6, no.2, 2007, pp.147-170.
13. Janus, J.M., Hortsman, H.Z., and Whitfield, D.L., "Unsteady Flowfield Simulation of Ducted Prop-Fan Configurations, Paper 92-0521, AIAA 30th Aerospace Sciences Meeting and Exhibit, Reno, Nevada, January 6-9, 1992.
14. Meyer, H.D. and Envia, E., "Aeroacoustic Analysis of Turbofan Noise Generation," NASA-CR 4715, 1999.
15. Kousen, K.A., "Eigenmode Analysis of Ducted Flows with Radially Dependent Axial and Swirl Components," CEAS/AIAA Paper 95-160, 1st CEAS/AIAA Aeroacoustics Conference, June 12-15, 1995, pp.1085-1094, Munich Germany.
16. Tweedt, D.L., "Computational Aerodynamic Simulations of an 840 ft/sec Tip Speed Advanced Ducted Propulsor Fan System Model for Acoustic Methods Assessment and Development," NASA/CR-2014-218129, October 2014.
17. Tweedt, D.L., "Preliminary Aerodynamic Investigation of Fan Rotor Blade Morphing," NASA, NASA/CR-2012-217815, December 2012.